

Geochemical Characteristics of the Middle Jurassic Coal-Bearing Mudstones in the Dameigou Area (Qaidam Basin, NW China): Implications for Paleoclimate, Paleoenvironment, and Organic Matter Accumulation

Kai Zhou, Jinyan Sun, Minfang Yang, Shuo Zhang, Weichao Wang, Ran Gao, Peixin Zhang, Wanqing Wang, Haoqing Liu, Longyi Shao, and Jing Lu*



Cite This: *ACS Omega* 2023, 8, 47540–47559



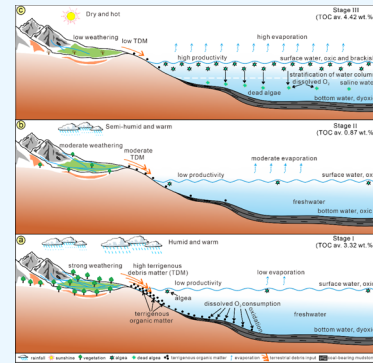
Read Online

ACCESS |

Metrics & More

Article Recommendations

ABSTRACT: The Qaidam Basin is a prominent oil and gas exploration and production base of NW China's Jurassic coal-bearing strata. Coal-bearing mudstones are important source rocks for unconventional reservoirs and can record valuable paleoenvironment and paleoclimate information. Here, geochemical analysis including total organic carbon (TOC), total sulfur, organic carbon isotopic composition, rock pyrolysis, X-ray diffraction, and major and trace elements were carried out on mudstone samples from the Middle Jurassic coal-bearing strata of the Dameigou section in the Qaidam Basin to reveal the paleoclimatic and paleoenvironmental conditions during the deposition of the strata and their controls on organic matter accumulation. Results show that the Middle Jurassic Dameigou and Shimengou formations include three significant stages based on their average TOC values of (3.32%, Stage I; 0.87%, Stage II; and 4.42%, Stage III) from the bottom to the top. The organic matter in mudstones in Stages I and II are mainly derived from terrestrial higher plants, while the organic matter has mixed sources of higher plant debris and lower aquatic organisms in Stage III. Paleoclimate parameters indicate that the mudstones in Stage I were deposited under humid and warm conditions, while the climate in Stage II changed to semiarid and warm conditions before turning dry and hot in Stage III. The varying paleoenvironmental characteristics under different paleoclimatic conditions have also been reconstructed. Our results suggest that the accumulation of organic matter in Stages I and II was primarily controlled by redox conditions, while paleoproductivity is the major controlling factor for organic matter accumulation in Stage III.



1. INTRODUCTION

Extensive research has confirmed the petroleum generation potential of coal-bearing strata.^{1–7} Coal-bearing source rocks refer to coal and associated carbonaceous/dark mudstone that can generate hydrocarbon. Commercial quantities of oil and gas have been discovered in the Jurassic coal-bearing mudstone sequences of NW China sedimentary basins, including the Tarim Basin, Qaidam Basin, Junggar Basin, Ordos Basin, and Turpan Basin.^{8–12} Coal-bearing mudstones not only are important source rocks for unconventional reservoirs but also record valuable information on the paleoenvironment and paleoclimate,^{13–16} receiving great attention in recent years.^{17–19}

The Qaidam Basin is a prominent oil and gas exploration and production base of NW China's Jurassic coal-bearing strata.^{20–22} According to the source correlation studies of oil and gas, the hydrocarbons are derived mainly from the Lower-Middle Jurassic coal-bearing mudstone sequences.^{21–24} Previous research related to the Lower-Middle Jurassic coal-bearing strata of the Qaidam Basin mainly focused on

provenance, sedimentary environment, sequence stratigraphy, and palynoflora characteristics.^{25–31} Although the organic geochemistry, source of organic matter, and hydrocarbon generation potential of the organic-rich shales of the Shimengou Formation (Callovian Stage) have been extensively studied in recent years,^{32–39} the geochemical characteristics of the coal-bearing mudstones in the Middle Jurassic Dameigou and Shimengou formations from the Aalenian to Callovian stages in the Qaidam Basin are rarely reported. In addition, little is known about the paleoenvironmental conditions as well as their influences on the organic matter accumulation of the coal-bearing mudstones during the Middle Jurassic.

Received: July 30, 2023

Revised: November 2, 2023

Accepted: November 14, 2023

Published: December 8, 2023



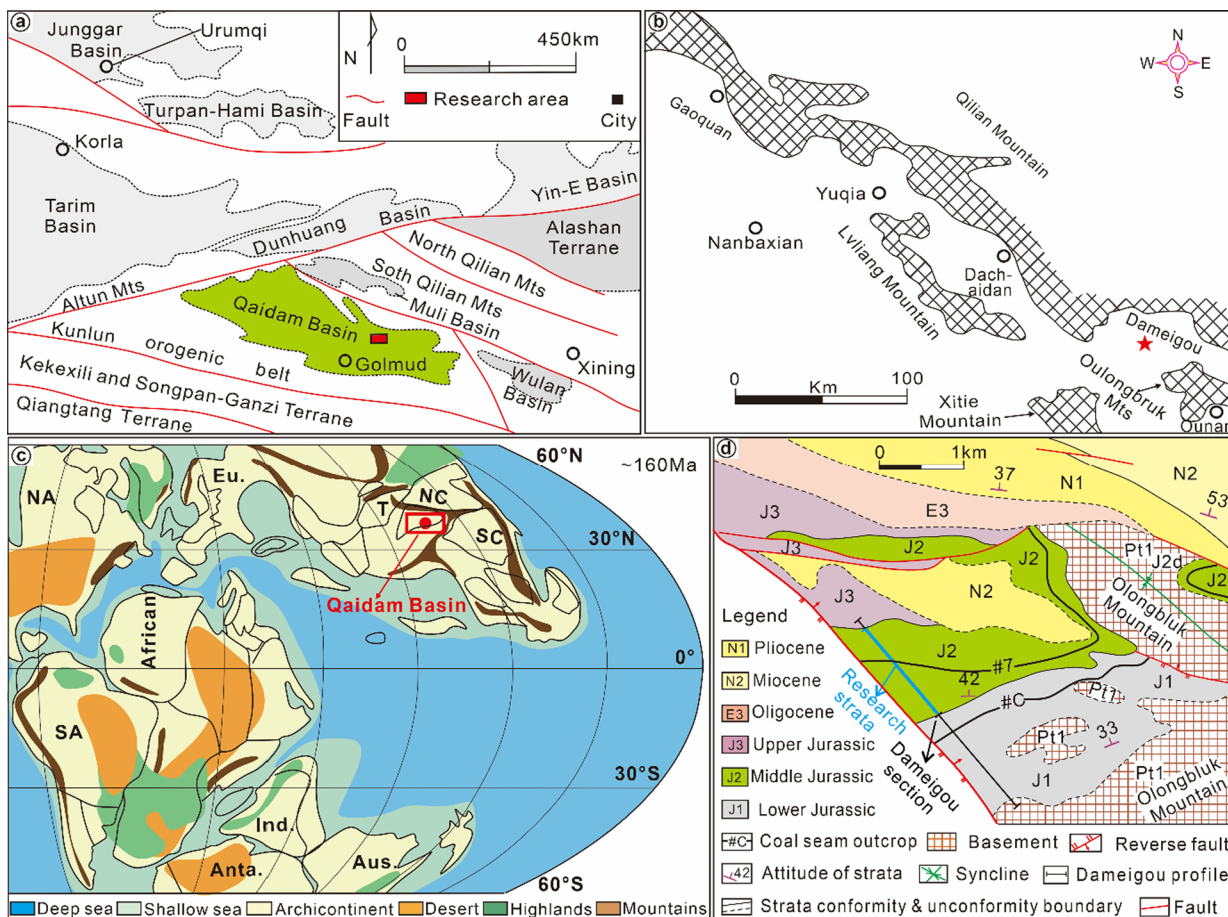


Figure 1. Location and the geological context for the Qaidam Basin. (a) Map showing tectonic setting for the Qaidam and adjacent sedimentary basins. (b) A sketch map showing the location of the Dameigou area. (c) Middle Jurassic paleogeographic map showing the approximate position of the Qaidam Basin. (d) Geological sketch of the Dameigou area showing the location of the Dameigou section. Abbreviations: Anta. – Antarctic Plate; Aus – Australian Plate; Eu. – European Plate; Ind. – Indian Plate; NA – North American Plate; NC – North China Plate; SA – South American Plate; SC – South China Plate; and T – Tarim Plate.

Here we investigate the Middle Jurassic coal-bearing strata using 57 fresh mudstone samples collected from the Dameigou and Shimengou formations of the Dameigou section in the Qaidam Basin, NW China. Data from total organic carbon (TOC), organic carbon isotopic composition ($\delta^{13}\text{C}_{\text{org}}$), kerogen macerals, Rock-Eval pyrolysis, mineral compositions, and elemental geochemistry are used to evaluate the source of organic matter and to quantify variations in paleoclimatic and paleoenvironmental conditions. We propose an evolution model to explain the mechanism of organic matter accumulation in the Middle Jurassic coal-bearing mudstones.

2. GEOLOGICAL SETTING

The Qaidam Basin, located at the northeast margin of the Qinghai–Tibet Plateau, is surrounded by the South Qilian Mountains to the north, the East Kunlun Mountains to the south, and the Altyn Mountains to the northwest (Figure 1a). The basin has an average elevation of around 3000 m and covers a total area of approximately $1.21 \times 10^5 \text{ km}^2$. It contains a 3–16 km-thick Mesozoic-Cenozoic nonmarine sedimentary succession unconformably overlying Precambrian crystalline basement lithologies.^{21,40–42} The northern Qaidam Basin (NQB), as one of the most significant coal- and oil-producing areas of the Qaidam Basin, covers an area of $\sim 3.4 \times 10^4 \text{ km}^2$ and is sandwiched between the Qilian and Qaidam plates. The

Dameigou area is located in the eastern part of the NQB (Figure 1b).

During the Middle Jurassic, the Qaidam Basin was a rift basin with a paleolatitude of about 30°N (Figure 1c).^{28,43,44} The sediment mainly came from the Qilian mountains to the north and the East Kunlun mountains to the south (Figure 1a).²⁸ The Dameigou area was one of the depositional centers in the NQB at that time, with organic-rich mudstones extensively deposited. The Middle Jurassic strata of the Dameigou area, represented by the Dameigou and Shimengou formations from the oldest to the youngest in time (Figure 2a), are our target strata. Based on previous sequence stratigraphic analysis and correlation of the basinal facies, the Dameigou Formation can be subdivided into a lower sand-conglomerate member (J_{2d^1}) and an upper coal-bearing member (J_{2d^2}) and the Shimengou Formation can be subdivided into a lower coal-bearing member (J_{2s^1}) and an overlying shale member (J_{2s^2}) (Figure 2a).³³

The sand-conglomerate member of the Dameigou Formation is dominated by conglomerate, coarse sandstone, mudstone, and occasional thin lines, representative of a fluvial depositional environment.^{25,45} The coal-bearing member of the Dameigou Formation is mainly composed of siltstone, mudstone, carbonaceous mudstone, and thick coal seams, which were deposited in a swampy, deltaic sedimentary

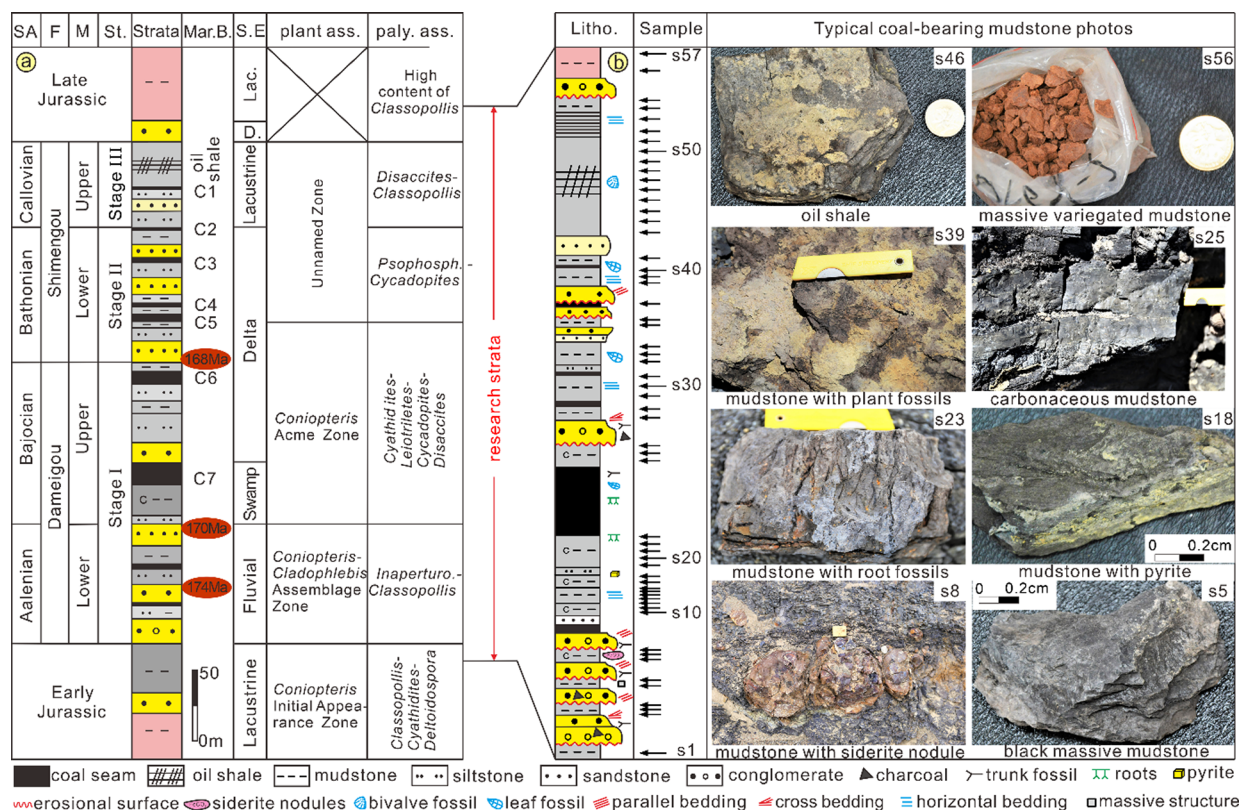


Figure 2. (a) Stratigraphy, palynological assemblages, vegetation, and sedimentary environment evolution of the Middle Jurassic of the northern Qaidam Basin. (b) Locations, lithology, and typical photos of the samples from the Dameigou section. Note: The coloring in the lithology column is similar to the natural colors of typical rocks found in strata. The coin in the mudstone photos is 2 cm in diameter. Abbreviations: D. – delta; F – Formation; Lac. – lacustrine; Litho. – lithology; M – member; Mar. B. – marker bed; paly. ass. – palynological assemblages; SA – series; St. – Stage; and S. E. – sedimentary environment.

system.^{25,45} The coal-bearing member of the Shimengou Formation consists of sandstone, siltstone, mudstone, and thin coal seams, representative of a depositional scenario in a deltaic environment. The shale member of the Shimengou Formation is composed of thick oil shale and mudstone that was deposited in a lake environment of various water depths. Based on biostratigraphy from fossil plants, sporopollen, and bivalves, the Dameigou Formation is dated to the Aalenian-Bajocian stage, while the Shimengou Formation has been dated to the Bathonian-Callovian stage (Figure 2a).^{25,26,30} These age assignments are also constrained by the youngest U-Pb dates of detrital zircon from sandstones at the bottom (174 Ma) and middle (170 Ma) of the Dameigou Formation and the bottom (168 Ma) of the Shimengou Formation (Figure 2a).^{28,46}

3. MATERIALS AND METHODS

A total of 57 fresh mudstone samples from the Middle Jurassic Dameigou and Shimengou formations were selected from the Dameigou section in the Qaidam Basin. Sampling locations are shown in Figure 2b. All samples were carefully packed before analysis and numbered consecutively from s1 to s57. Individual samples were first broken down to a diameter of less than 1 mm and then divided into two parts. One part was prepared for kerogen enrichment and identification according to the China National Standard (SY/T 5125–2014), with no less than 300 effective points per sample analyzed. The remaining part was further crushed to a size smaller than 200 μm and divided into seven subparts for mineral composition analysis,

TOC analysis, total sulfur (TS) analysis, $\delta^{13}\text{C}_{\text{org}}$ analysis, major element analysis, trace element analysis, and pyrolysis.

Mineral composition analysis was performed by an X-ray diffractometer (XRD; D/max 2500 PC) with Cu-K α radiation. The sample powders were pressed into a sample frame evenly. The XRD patterns were recorded over a 2θ interval of 3–70°, and the data were interpreted using Rockquan 2016 software with a precision better than $\pm 5\%$. TOC values were measured using a carbon–sulfur analyzer (CSS80-A) with a lower detection limit of 100 mg/g and an absolute analysis error of $\pm 0.2\%$. TS analysis was performed using a carbon–sulfur analyzer (Eltra CS580-A) with a lower detection limit of 30 ppm, yielding an analytical accuracy within 5% of the reported values. Pyrolysis was conducted using a Rock-Eval pyrolysis instrument, which provides free hydrocarbon amount (S_1), the remaining hydrocarbon amount (S_2) and the pyrolytic temperature corresponding to the generated maximum remaining hydrocarbon (T_{\max}). $\delta^{13}\text{C}_{\text{org}}$ analysis was performed using a stable isotope mass spectrometer (MAT253), and $\delta^{13}\text{C}_{\text{org}}$ values were expressed in per mil (‰) with respect to the Vienna Pee Dee Belemnite (VPDB) standard, with an absolute analytical error of $\pm 0.1\%$. Major element analysis was undertaken with an X-ray fluorescence spectrometer (PW2404) with a precision better than $\pm 5\%$. Trace element analysis was undertaken using an inductively coupled plasma mass spectrometer (Finnigan MAT) with a relative analytical error better than $\pm 5\%$. Kerogen maceral identification and mineral compositions were analyzed at the State Key Laboratory Coal Resources and Safe

Table 1. Total Organic Carbon, Organic Carbon Isotope Composition, Total Sulfur, Kerogen Macerals, and Rock-Eval Pyrolysis Results of Mudstones in the Study Area

sample no.	TOC (%)	$\delta^{13}\text{C}_{\text{org}}$ (‰)	TS (%)	vitrinite (%)	exinite (%)	inertinite (%)	sapropelinite (%)	T_{max} (°C)	S_1 (mg/g)	S_2 (mg/g)	S_3 (mg/g)	$S_1 + S_2$ (mg/g)	HI (mg HC/g TOC)
s1	0.36	-24.9	0.09	75.5	2.5	18.9	3.1						
s2	2.61	-23.3	0.11	73	2.8	20.7	3.4	442	0.12	2.64	0.57	2.76	72
s3	2.52	-22.1	0.03										
s4	2.29	-22.2	0.04										
s5	2.81	-22.4	0.05										
s6	2.92	-22.1	0.03	65.7	5.4	26.3	2.5						
s7	4.71	-21.7	0.06	66	4.3	26.4	3.3						
s8	4.73	-22.1	0.01										
s9	4.78	-22.7	0.09										
s10	3.12	-22.3	0.03	56.9	15.5	22.5	5.1	440	0.12	2.91	1.24	3.03	82
s11	3.72	-22.1	0.06	75.6	10.7	13.5	0.3						
s12	3.65	-21.0	0.08	81.1	7.4	11.2	0.3						
s13	3.45	-22.0	0.09	78.4	6.2	13.8	1.6	440	0.05	3.48	0.63	3.53	53
s14	2.90	-21.1	0.04	77.2	5.1	15.8	1.9						
s15	4.14	-23.3	0.23	79.7	6.1	14.2	0						
s16	3.82	-21.0	0.13	77.8	3.8	16.5	1.9						
s17	3.02	-21.9	0.17	78.7	4.4	12.2	4.7						
s18	3.73	-21.5	0.08	71	5.7	18.9	4.4						
s19	3.78	-21.0	0.05	71	2.6	23.4	3	438	0.05	3.81	0.53	3.86	82
s20	4.38	-22.7	0.01	73.8	4	16.8	5.4						
s21	3.64	-21.5	0.07	73.7	1.7	17	7.6						
s22	2.67	-21.6	0.04	71.9	4.5	18.5	5.1						
s23	3.69	-21.9	0.01	69.5	5.1	22	3.4						
s24	2.15	-24.0	0.03	72.8	6	21.2	0						
s25	2.01	-24.5	0.01	74.3	3.8	17.8	4.1						
s26	1.80	-24.2	0.01										
s27	0.65	-22.4	0.01	69.2	13.6	8.9	8.3						
s28	0.61	-22.3	0.02										
s29	0.63	-22.1	0.09	72.4	10.8	15	1.8	442	0.03	0.11	0.13	0.14	67
s30	0.40	-22.0	0.02										
s31	0.43	-22.3	0.07										
s32	0.45	-22.6	0.05	68	13.9	14.2	3.9	442	0.01	0.07	0	0.08	83
s33	0.78	-22.4	0.03										
s34	0.84	-22.6	0.09	64.8	15.9	15.9	3.5						
s35	0.86	-22.1	0.11										
s36	0.92	-22.3	0.12	74.8	2.5	20.8	1.9						
s37	1.01	-21.6	0.06										
s38	1.36	-21.5	0.08	79.1	2.6	15.1	3.2						
s39	1.13	-22.6	0.05	81.7	2.9	12.8	2.6	440	0.04	0.23	0.37	0.27	96
s40	1.52	-23.1	0.03	86.1	1.4	10.1	2.3						
s41	1.50	-22.4	0.02	89.4	1.8	7.3	1.5	438	0.01	0.22	0.23	0.23	101
s42	4.38	-26.0	0.15	26.6	3.4	1.6	68.3						
s43	4.00	-26.1	0.27	31.1	1.8	2.5	64.6	438	0.08	9.75	0.81	9.83	324
s44	4.27	-26.1	0.25	32.4	3.1	3.6	60.9						
s45	5.00	-25.0	0.34	31.3	1.8	2	64.9						
s46	4.14	-25.1	0.41	29.6	2.3	2.6	65.5						
s47	4.90	-26.1	0.32	23.5	2.5	3.7	70.4	438	0.14	14.06	2.1	14.2	297
s48	4.98	-25.5	0.45	26.2	1.9	4	67.9						
s49	4.97	-25.3	0.28	27.2	1.7	1.9	69.2						
s50	4.44	-25.1	0.3	5.6	3.1	3.6	87.8						
s51	4.43	-24.8	0.33	24	2.3	2.9	70.8	435	0.03	14.96	1.63	14.99	532
s52	4.37	-24.2	0.32										
s53	4.10	-23.3	0.42										
s54	3.98	-23.0	0.35	34.5	3.7	6.5	55.4	429	0.13	9.49	0	9.62	243
s55	3.95	-22.8	0.31	41.1	3.5	13.5	42						
s56	0.40	-25.5	0.31	55	5.3	7.6	32.2						
s57	0.32	-25.8	0.1	74.2	1.6	21	3.2						

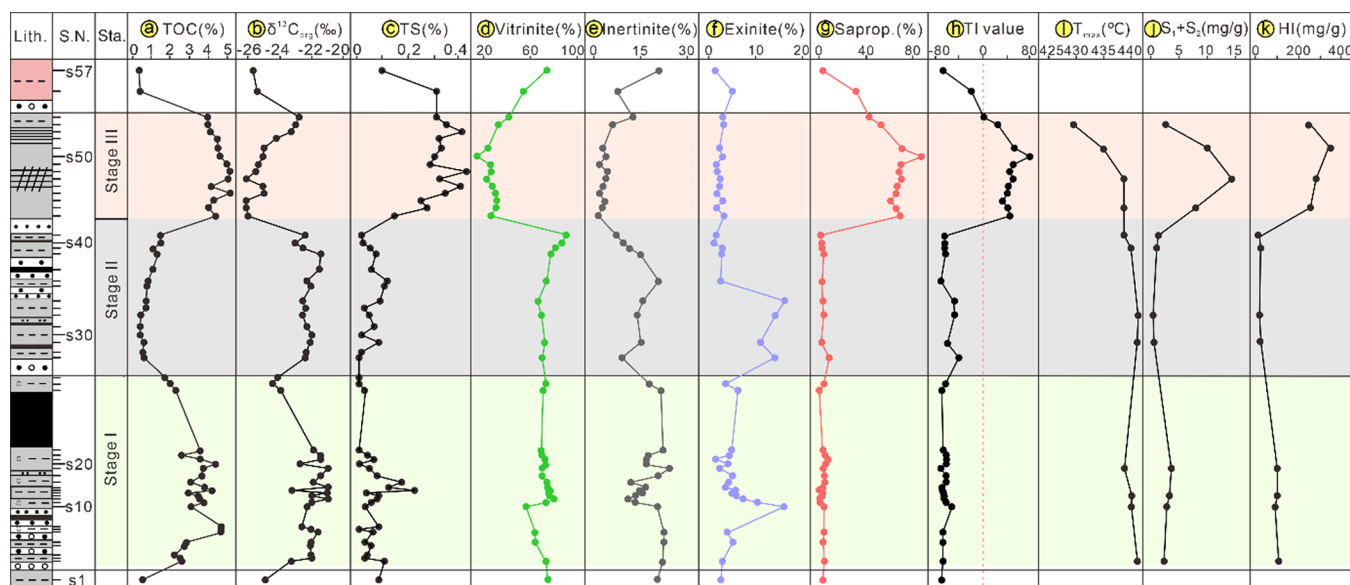


Figure 3. Analytical result of TOC, $\delta^{13}\text{C}_{\text{org}}$, TS, kerogen macerals, TI values, and Rock-Eval pyrolysis for mudstone samples in the study area. Abbreviations: Litho. – lithology; S.N. – sample number; Sta. – Stage; and Saprop. – spropelinite.

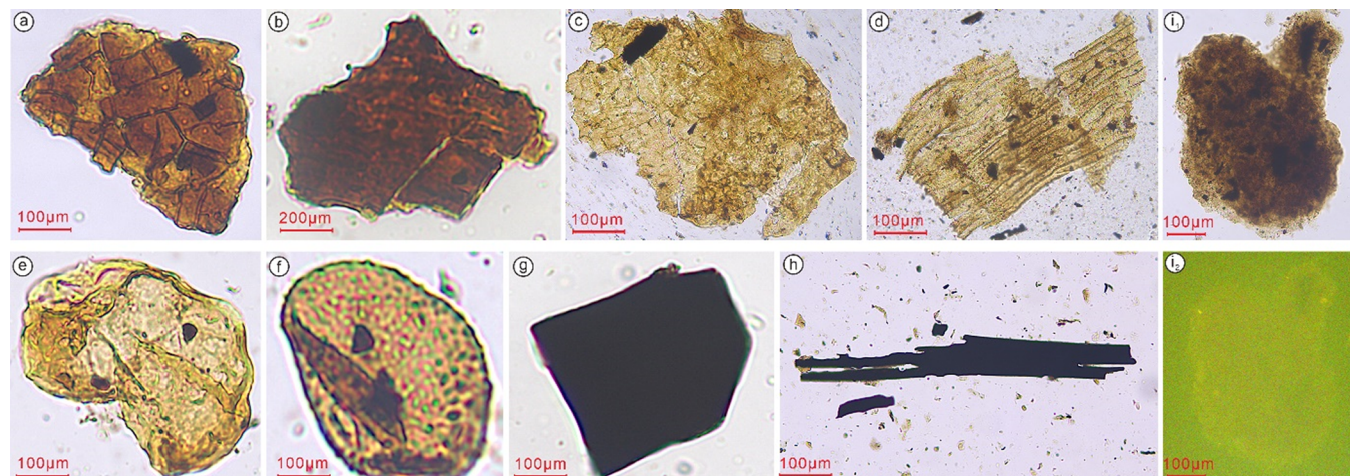


Figure 4. Micrographs showing the microstructure of kerogen macerals in the study area: (a, b) telinite with clear wood structure (transmitted light, samples s40 and s41); (c, d) suberinite (transmitted light, samples s32 and s34); (e, f) sapropelinite (transmitted light, sample s49); (g, h) inertinite (transmitted light, sample s19); and (i₁–i₂) amorphous (transmitted light and fluorescence, respectively, sample s46).

Mining (Beijing), and major and trace elements were analyzed at the Beijing Research Institute of Uranium Geology. TOC analysis and pyrolysis were conducted at the Research Institute of Petroleum Exploration and Development (Beijing).

The kerogen type index (TI) can be calculated using the following formula:⁴⁷

$$\text{TI} = (a + 0.5b - 0.75c - d) \times 100 \quad (1)$$

where a represents the contents of amorphous kerogen, b represents exinite content, c represents vitrinite content, and d represents inertinite content (SY/T 5125-2014).

From the major and trace element analysis, the chemical index of alteration (CIA), the weathering index of Parker (WIP), and the C-value are calculated as follows, where all oxides are in molar units in eqs 2 and 3 and the elemental contents are in ppm in eq 4.^{48–50}

$$\text{CIA} = \text{Al}_2\text{O}_3 / (\text{Al}_2\text{O}_3 + \text{CaO}^* + \text{Na}_2\text{O} + \text{K}_2\text{O}) \times 100 \quad (2)$$

$$\begin{aligned} \text{WIP} = & (2\text{Na}_2\text{O}/0.35 + \text{MgO}/0.9 + 2\text{K}_2\text{O}/0.25 \\ & + \text{CaO}^*/0.7) \times 100 \end{aligned} \quad (3)$$

where CaO^* represents the CaO in detrital components; $\text{CaO}^* = (\text{CaO} - \text{P}_2\text{O}_5 \times 10/3)$ if CaO^* content is lower than that of Na_2O ; otherwise, CaO^* is equal to the content of Na_2O .⁵¹

$$\begin{aligned} \text{Cvalue} = & \Sigma(\text{Fe} + \text{Mn} + \text{Cr} + \text{Ni} + \text{V} + \text{Co}) \\ & / \Sigma(\text{Ca} + \text{Mg} + \text{Sr} + \text{Ba} + \text{K} + \text{Na}) \end{aligned} \quad (4)$$

The Al-normalized enrichment factors (EFs) of element concentrations are extensively used as a proxy for estimating elemental enrichment and depletion since Al originated from aluminosilicate in terrigenous detrital minerals and is resistant to weathering.^{52,53} The EF of elements can be calculated using the following equation:⁵²

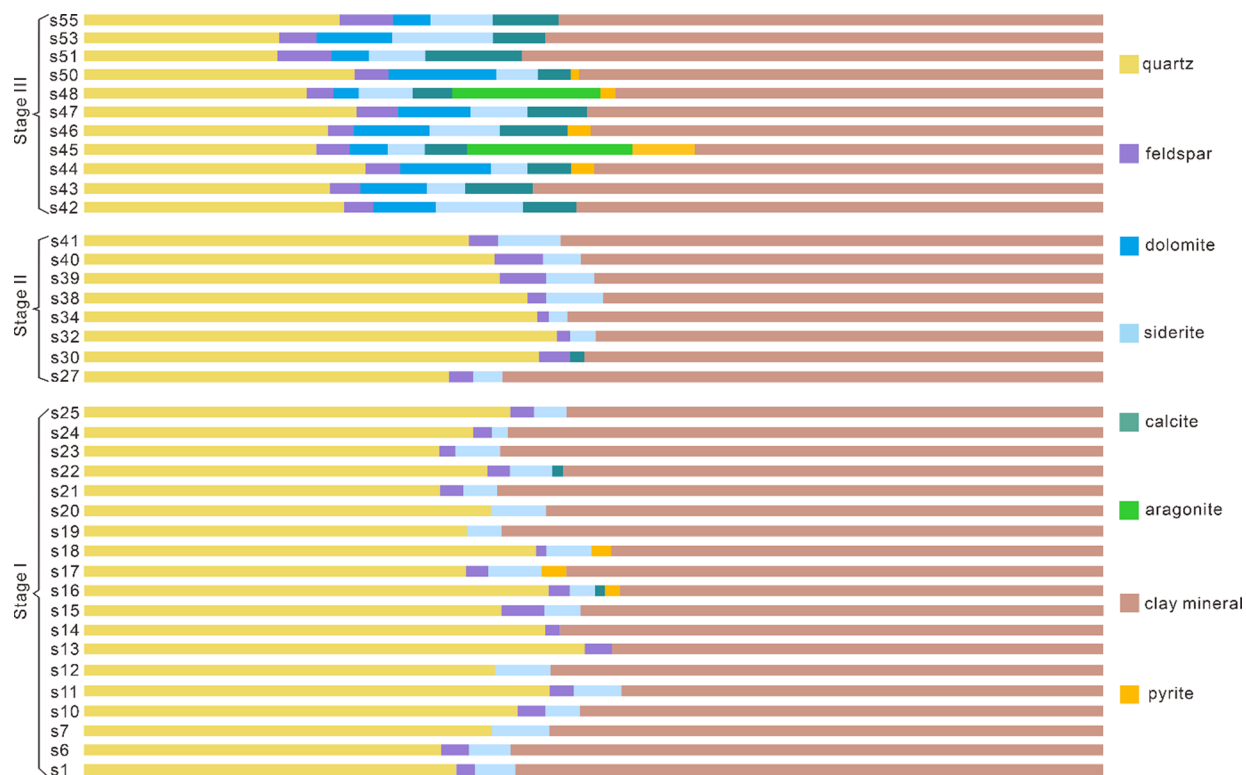


Figure 5. Mineral composition of the mudstone samples from the Dameigou and Shimengou formations.

$$E_{EF} = (E/Al)_{\text{sample}} / (E/Al)_{\text{average shale}} \quad (5)$$

where the Post-Archean average Australian Shale is used as a normalization standard.⁵⁴

4. RESULTS

4.1. TOC, $\delta^{13}\text{C}_{\text{org}}$, and TS. Results for the TOC, $\delta^{13}\text{C}_{\text{org}}$, and TS analysis are shown in Table 1 and Figure 3a–c. TOC values vary from 0.32 to 5.0%, with an average value of 2.79% (Figure 3a). Three significant stages, which are named Stages I, II, and III with different TOC values, are recognized in the studied strata (Figure 3a). Stage I corresponding to the Dameigou Formation (Aalenian-Bajocian stage) is characterized by high TOC values (\bar{x} (mean) = 3.32%), Stage II corresponding to the coal-bearing member of the Shimengou Formation (Bathonian stage) is distinguished by low TOC values (\bar{x} = 0.87%), while Stage III corresponding to the shale member of the Shimengou Formation (Callovian stage) has high TOC values again (\bar{x} = 4.42%). $\delta^{13}\text{C}_{\text{org}}$ values vary from -26.1 to -21.0‰ (\bar{x} = -23.3‰) (Figure 3b), with an average value of -22.2, -22.3, and -24.9‰ in Stages I, II, and III, respectively. TS values vary from 0.01 to 0.45%, with an average value of 0.13% (Figure 3c).

4.2. Kerogen Macerals and Rock-Eval Pyrolysis Parameters. Results on kerogen macerals and Rock-Eval pyrolysis are shown in Figure 3d–k and Table 1. Vitrinite varies from 5.6 to 89.4% (\bar{x} = 60.7%) and has higher values in Stages I and II and lower values in Stage III (Figures 3d and 4a,b). Inertinite varies from 1.6 to 26.4% (\bar{x} = 13.1%, Figures 3e and 4g,h) and exinite varies from 1.4 to 15.9% (Figures 3f and 4c,d). Both inertinite and exinite show trends similar to that of vitrinite in the three stages (Figure 3d–f). Ssapropelinite has a uniformly low content from Stage I to Stage II, with an average value of 3.1% (Figures 3g and 4e,f). In Stage III,

sapropelinite has higher content varying from 42.0 to 87.8% (\bar{x} = 65.6%). TI values are within 0–40 in Stage I, more than 70 in Stage II, and less than 0 in Stage III (Figure 3h). The T_{max} of the organic matters from the Dameigou and Xiaomeigou formations varies from 428 to 442 °C with an average of 438.5 °C (Figure 3i). The total genetic potential of hydrocarbons ($S_1 + S_2$) varies from 0.08 to 4.99 mg/g (\bar{x} = 5.21 mg/g, Figure 3j), and the hydrogen index (HI = S_2/TOC) varies from 14.7 to 377.7 mg hydrocarbon (HC)/g TOC with an average value of 130.9 mg HC/g TOC (Figure 3k).

4.3. Mineral Compositions. Results of mineral compositions are plotted in Figure 5 and tabulated in Table 2. XRD results show that clay minerals (40.2–59.7%, \bar{x} = 53.2%) are the most abundant minerals in the Middle Jurassic Dameigou and Shimengou formation mudstones, followed by quartz, siderite, feldspar, dolomite, calcite, aragonite, and pyrite (Table 2). Similar mineral compositions are found in Stages I and II, with a high proportion of clay minerals and quartz and a minor amount of siderites and feldspars (Figure 5). Stage III is characterized by a high content of clay minerals, a medium content of quartz and carbonate minerals (including calcite, dolomite, aragonite, and siderite), and low contents of feldspar and pyrite (Figure 5).

4.4. Element Geochemistry. The concentrations of major element oxides in the mudstone samples from the Dameigou and Shimengou formations are listed in Table 3. The major chemical compositions are SiO_2 , Al_2O_3 , CaO , Fe_2O_3 , MgO , K_2O , and Na_2O . EF results show that SiO_2 , Al_2O_3 , and TiO_2 are enriched and other elements are depleted in the mudstones of Stages I and II (Figure 6a). In Stage III, CaO is enriched, and other elements are depleted in the mudstone samples. Analytical results of the trace elements show that Ba, Rb, Sr, V, Cr, Zn, and Zr are the most abundant trace elements (with average values higher than 50 ppm) in the Dameigou and

Table 2. Bulk Minerals (%) of the Mudstone Samples in the Study Area

sample no.	bulk minerals (%)							
	clay minerals	quartz	feldspar	calcite	dolomite	siderite	aragonite	pyrite
s1	58.2	36.7	1.3	0	0	3.8	0	0
s6	58.7	34.8	2.6	0	0	3.9	0	0
s7	54.8	39.9	0	0	0	5.3	0	0
s10	51.9	42.3	2.4	0	0	3.4	0	0
s11	47.5	46.3	2.2	0	0	4.0	0	0
s12	54.9	40.3	0	0	0	4.8	0	0
s13	48.4	49.3	2.3	0	0	0	0	0
s14	53.8	45.0	1.2	0	0	0	0	0
s15	52.0	41.2	3.8	0	0	3.0	0	0
s16	47.5	45.9	2.0	0.7	0	2.2	0	1.7
s17	53.2	37.3	2.2	0	0	5.0	0	2.3
s18	58.3	34.3	0.7	0	0	4.6	0	2.1
s19	58.7	37.5	0	0	0	3.8	0	0
s20	55.1	39.9	0	0	0	5.0	0	0
s21	59.7	34.8	2.2	0	0	3.3	0	0
s22	53.2	39.6	2.1	1.1	0	4.0	0	0
s23	59.6	34.8	1.1	0	0	4.5	0	0
s24	58.9	38.7	1.3	0	0	1.1	0	0
s25	53.0	41.8	2.1	0	0	3.1	0	0
s27	59.2	36.1	2.1	0	0	2.6	0	0
s30	51.4	44.5	3.2	0.9	0	0	0	0
s32	49.9	46.1	0.9	0	0	3.1	0	0
s34	52.9	44.9	0.8	0	0	1.4	0	0
s38	48.9	43.7	1.3	0	0	6.1	0	0
s39	50.0	40.9	4.5	0	0	4.6	0	0
s40	51.5	40.2	4.9	0	0	3.4	0	0
s41	53.2	36.8	3.6	0	0	6.4	0	0
s42	52.3	26.4	1.7	5.5	5.7	8.4	0	0
s43	56.7	23.6	2.6	6.9	6.6	3.6	0	0
s44	50.2	27.3	3.6	4.0	8.9	3.9	0	2.1
s45	40.2	22.2	3.7	4.0	3.9	3.8	16.1	6.1
s46	50.6	23.4	2.3	7.1	7.4	6.9	0	2.3
s47	51.2	26.9	2.7	5.6	8.3	5.3	0	0
s48	48.1	22.1	2.1	5.4	2.0	4.2	14.6	1.5
s50	51.6	26.0	3.4	4.0	10.2	4.2	0	0.6
s51	57.2	17.6	4.2	9.7	6.1	5.2	0	0
s53	55.1	18.3	4.3	4.9	7.4	10.0	0	0
s55	54.2	24.6	5.4	5.8	3.9	6.1	0	0

Shimeigou formation mudstones, followed by Sc, Co, Ni, B, Ga, Th, U, Mo, Cu, Cs, Ta, Hf, Nb, and Y (Table 4). As shown in Figure 6b, V, Cr, Ce, Ni, Cu, Zn, Rb, Sr, and Ba are all depleted in the mudstones of Stages I and II, whereas Y, Th, U, and Sc are enriched in these mudstones. However, in Stage III mudstones, Cu, Zn, Sr, and U are enriched, and V, Cr, Ce, Ni, Rb, Y, Ba, Th, and Zr are depleted.

Results for representative paleoclimatic and paleoenvironmental proxies of the mudstone samples from the Dameigou and Shimeigou formations are shown in Figure 7 and Table 5. The C value varies between 0.19 and 0.87, and decreases from Stage I to Stage III (Figure 7a). Rb/Sr ratios vary from 0.29 to 2.51 and resemble the trend of the C value (Figure 7b). CIA values vary from 60.3 to 92.1 and decreases gradually from Stage I to Stage III (Figure 7c). WIP values are between 13.8 and 51.7 and show an increasing trend from Stage I to Stage III (Figure 7d). Zr/Al ratios vary from 4.13 to 14.88 (Figure 7e) and Ti/Al ratios vary from 0.03 to 0.08 (Figure 7f). Both Zr/Al and Ti/Al ratios show a decreasing trend from Stage I to Stage III. V/(V + Ni) ratios vary from 0.52 to 0.84 and have a value

interval ($\bar{x} = 0.58$) in Stage II that is lower than those in Stages I and III (Figure 7g). U_{EF} and Mo_{EF} values vary from 1.25 to 8.72 and 0.34 to 9.38, respectively, with similar shapes with that of the V/(V + Ni) ratios (Figure 7h,i). P/Al ratios vary from 18.2×10^{-4} to 169.9×10^{-4} (Figure 7j), and Ba/Al ratios vary from 10.68 to 42.11 (Figure 7k). Both P/Al and B/Al ratios show intermediate values in Stage I, low values in Stage II, and high values in Stage III. Sr/Ba ratios vary from 0.16 to 1.13 (Figure 7l), which shows low values in Stages I and II and high values in Stage III. B/Ga ratios vary from 0.60 to 4.38 (Figure 7m) and show the same general trends as for Sr/Ba ratios. In the present analysis data from geochemical parameters are new, whereas the TOC values, TS values, $\delta^{13}\text{C}_{\text{org}}$ values, and kerogen macerals come from ref 27.

5. DISCUSSION

5.1. Organic Matter Source. Kerogen type provides qualitative information about organic matter sources.^{54,55} The kerogen types are typically classified into types I, II, and III. Type I kerogen is composed dominantly of alginite and is

Table 3. Major Element Content (%) in the Mudstone Samples in the Study Area

sample no.	SiO ₂	Al ₂ O ₃	Fe ₂ O ₃	MgO	CaO	Na ₂ O	K ₂ O	MnO	TiO ₂	P ₂ O ₅
s1	55.05	15.30	6.60	1.120	0.297	0.569	2.83	0.021	0.836	0.039
s2	54.76	12.90	3.40	0.534	0.217	0.156	1.68	0.007	0.674	0.043
s3	53.15	12.20	7.78	0.528	0.290	0.476	1.76	0.009	0.712	0.048
s4	52.22	11.40	7.21	0.498	0.370	0.215	2.01	0.011	0.697	0.041
s5	50.08	12.60	8.22	0.513	0.540	0.187	1.93	0.003	0.775	0.046
s6	53.15	12.30	8.34	1.050	0.706	0.420	1.96	0.050	1.040	0.035
s7	55.31	18.30	1.21	0.593	0.860	0.198	1.72	0.004	0.982	0.055
s8	52.18	15.70	1.09	0.324	0.360	0.209	1.58	0.006	0.876	0.067
s9	53.57	18.80	2.14	0.245	0.210	0.214	1.25	0.035	0.834	0.056
s10	52.12	13.60	5.09	0.177	0.310	0.267	1.69	0.034	0.850	0.043
s11	55.61	19.25	0.97	0.547	0.172	0.116	1.76	0.004	0.786	0.085
s12	56.06	20.26	10.19	0.332	0.260	0.090	1.65	0.055	0.878	0.078
s13	56.93	19.11	1.71	0.417	0.126	0.106	1.75	0.006	0.849	0.084
s14	55.25	18.70	1.47	0.437	0.213	0.201	1.33	0.006	0.786	0.037
s15	51.63	18.77	1.64	0.505	0.350	0.439	1.86	0.006	0.875	0.045
s16	53.56	12.50	6.03	0.588	0.275	0.093	1.56	0.161	0.881	0.044
s17	57.98	23.37	1.32	0.646	0.194	0.199	1.46	0.005	0.992	0.063
s18	52.94	15.68	5.89	0.388	0.147	0.162	1.66	0.027	0.858	0.073
s19	58.30	22.25	3.65	0.371	0.141	0.125	1.35	0.016	0.830	0.056
s20	59.24	24.50	0.95	0.503	0.192	0.126	1.58	0.007	0.982	0.064
s21	49.87	15.21	4.89	0.437	0.156	0.121	1.64	0.025	0.825	0.088
s22	45.74	25.93	0.93	0.458	0.408	0.081	1.78	0.021	0.933	0.078
s23	57.98	25.79	1.22	0.689	0.159	0.393	1.76	0.007	0.977	0.061
s24	51.37	22.70	0.78	0.388	0.201	0.081	1.65	0.004	0.881	0.089
s25	58.63	20.50	2.14	0.525	0.607	0.201	1.75	0.011	0.835	0.065
s26	59.23	20.30	2.16	0.564	0.159	0.265	1.77	0.012	0.889	0.083
s27	59.18	23.51	2.23	0.796	0.143	0.725	2.71	0.008	0.908	0.078
s28	59.03	25.30	2.47	0.798	0.218	0.408	2.45	0.012	0.874	0.048
s29	57.86	23.40	2.35	0.886	0.179	0.616	2.78	0.009	0.912	0.057
s30	61.46	20.27	2.63	0.898	0.135	0.643	2.37	0.007	0.889	0.043
s31	66.38	15.10	3.17	0.943	0.213	0.632	2.84	0.018	0.886	0.041
s32	55.48	19.79	6.54	1.050	2.320	0.486	2.47	0.090	0.853	0.073
s33	57.35	23.40	4.21	1.030	0.079	0.578	2.63	0.022	0.913	0.059
s34	50.05	25.27	1.74	1.150	0.078	0.581	2.87	0.010	0.943	0.046
s35	54.78	24.30	1.78	1.050	0.096	0.544	2.76	0.019	0.816	0.058
s36	57.19	22.40	3.09	0.892	0.134	0.497	2.62	0.027	0.798	0.066
s37	56.57	23.60	2.13	0.987	0.089	0.512	2.79	0.031	0.756	0.074
s38	57.39	24.22	1.88	0.996	0.078	0.485	2.68	0.010	0.813	0.085
s39	54.41	21.27	6.22	0.917	0.150	0.525	2.72	0.071	0.904	0.089
s40	55.55	21.67	1.12	0.450	0.276	0.431	2.83	0.006	0.691	0.085
s41	55.87	20.88	2.36	0.447	0.429	0.514	2.59	0.007	0.876	0.085
s42	53.05	16.47	5.45	1.350	0.711	0.709	2.37	0.056	0.519	0.165
s43	49.10	13.16	4.39	1.260	1.654	0.791	2.50	0.034	0.479	0.145
s44	44.66	11.09	4.43	1.360	0.951	0.743	2.58	0.027	0.463	0.157
s45	53.36	15.10	4.58	0.079	2.186	0.766	2.43	0.025	0.454	0.160
s46	44.71	20.56	3.17	1.420	1.096	0.863	2.65	0.169	0.635	0.173
s47	42.91	20.12	3.77	1.480	0.990	0.981	2.36	0.022	0.576	0.229
s48	52.69	20.08	3.10	1.210	2.185	0.606	2.46	0.025	0.611	0.228
s49	48.16	21.30	3.40	1.310	1.312	0.688	2.41	0.042	0.596	0.241
s50	51.29	20.40	3.10	1.270	1.636	0.722	2.23	0.097	0.631	0.206
s51	47.28	19.35	3.27	1.380	1.340	1.010	2.52	0.069	0.624	0.200
s52	45.23	12.30	8.12	1.260	2.465	1.040	2.64	0.028	0.511	0.209
s53	51.48	13.10	8.66	2.430	1.700	1.050	2.32	0.035	0.561	0.176
s54	47.57	11.20	5.76	1.410	1.267	1.210	2.35	0.021	0.445	0.134
s55	46.36	11.76	3.84	1.390	1.585	1.150	2.69	0.014	0.462	0.144
s56	51.93	12.10	5.92	2.070	0.503	1.770	2.86	0.022	0.707	0.085
s57	52.30	13.30	7.72	2.820	4.820	1.620	2.91	0.102	0.658	0.082

primarily produced in situ in water. Type III kerogen is derived principally from terrestrial higher plants, whereas type II

kerogen commonly has a mixed source of higher plant debris and lower aquatic organisms.^{56,57} There are many evaluation

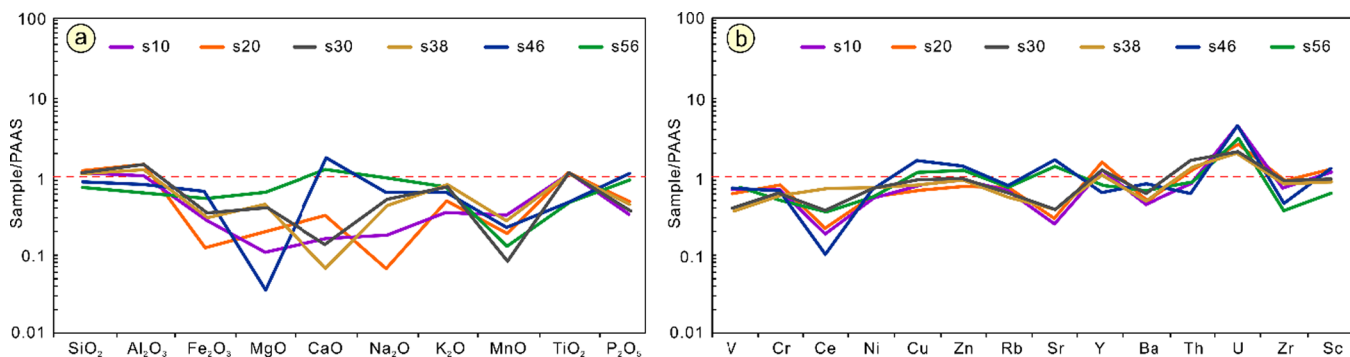


Figure 6. PAAS-normalized major and some trace element distributions of the Middle Jurassic coal-bearing mudstones from the Dameigou section. (a) Major elements; (b) some trace elements.

indexes of organic matter types, such as TI, $\delta^{13}\text{C}$, as well as HI.^{58–60} Specifically, TI values <0, 0–80, and >80 correspond to type III, type II, and type I kerogen, respectively.⁴⁷ The $\delta^{13}\text{C}$ values of type I, type II, and type III kerogens are usually less than $-26.5\text{\textperthousand}$, between -26.5 and $-25\text{\textperthousand}$, and greater than $-25\text{\textperthousand}$, respectively.^{61,62}

In this study, we use the TI values, $\delta^{13}\text{C}_{\text{org}}$, and the HI versus T_{max} plot to evaluate kerogen types. According to the HI versus T_{max} plots (Figure 8a), the studied samples from Stages I and II fall into the type III kerogen zone, whereas the samples from Stage III fall into the type II kerogen zone. The TI values (Figure 3h) in Stages I and II are less than 0, indicating type III kerogen. In Stage III, except for one sample (s52) with a value of 81.6, the TI values are all between 0 and 80, indicating type II kerogen. In addition, the $\delta^{13}\text{C}_{\text{org}}$ values of the kerogen in Stages I and II are between -24.5 and $-21.0\text{\textperthousand}$, with an average of $-22.3\text{\textperthousand}$, falling into the range of type III kerogen. The kerogens in Stage III have $\delta^{13}\text{C}_{\text{org}}$ values ranging from -26.1 to $-22.8\text{\textperthousand}$, which mostly fall in the range of type II kerogen (Figure 3b). Based on the analysis above, we can infer that the organic matter of Stages I and II is mainly derived from terrestrial higher plants, while the organic matter has mixed sources of higher plant debris and lower aquatic organisms in Stage III.

5.2. Paleoclimatic Conditions. The distribution and relative concentrations of climate-sensitive elements in mudstones provide clues to paleoclimatic conditions.⁶³ Fe, Mn, V, Ni, Cr, and Co are commonly enriched in sediments under humid conditions, while Ca, Mg, Na, K, Sr, and Ba are linked to larger water alkalinity owing to evaporation under arid conditions.⁶⁴ The C value, which is the ratio of total molar concentrations of the two types of elements, has been widely employed as a paleoclimate indicator.^{64,65} High C values (>0.6) represent humid conditions, while low C values (<0.4) indicate arid climatic conditions.⁶⁶ Additionally, the Rb/Sr ratio is also a proxy for paleoclimate in lacustrine fine-grained siliciclastic sediments.^{67,68} Rb is easily adsorbed by clay minerals, while Sr can migrate readily during diagenesis for its higher solubility.⁶⁹ Under arid climate conditions with decreasing precipitation and weathering intensities, the abundance of Sr in sediments increases, resulting in a decrease in the Rb:Sr ratio in sedimentary rocks. Therefore, high Rb/Sr ratios reflect humid climates, and low values reflect an arid climate.⁷⁰

In the study area, the C value shows higher values (0.57–0.87, $\bar{x} = 0.64$) in Stage I, medium values in Stage II (0.36–0.54, $\bar{x} = 0.45$), and lower values in Stage III (0.19–0.36, $\bar{x} =$

0.30, Figure 7a), indicating humid, semihumid, and semiarid to arid conditions, respectively. Meanwhile, Rb/Sr ratios show a decreasing trend from Stage I to Stage III (Figure 7b), which implies that the Dameigou area underwent climate aridification during the Middle Jurassic. Meanwhile, the palynological assemblages show a decrease in pteridophyte spores and an increase in gymnosperm pollen from the Dameigou Formation to the Shimengou Formation, suggesting a transition from humid to arid conditions.^{25–27} Additionally, the lithologies, palynological records, and geochemical parameters in other basins of NW China also suggest a humidity decrease from the Aalenian stage to the Callovian stage.^{71–73}

A climate pattern of humid-warm and dry-hot in the Qadiam Basin during the Middle Jurassic has been proposed by previous studies on the basis of sedimentary characteristics, palynological assemblages, and geochemical indexes.^{26,38,74,75} Based on the geochemical results in this study, we suggest that the Dameigou area experienced a climatic evolution from humid and warm in Stage I, to semihumid and warm in Stage II, and then to dry and hot in Stage III.

5.3. Weathering Degree. CIA and WIP have been extensively used to evaluate the weathering intensity of silicate rocks in the provenance area based on the proportions of alkali and alkaline earth elements in weathered products.^{76–79} Stronger chemical weathering results in higher CIA values and lower WIP values.^{49,80} Generally, low CIA values (50–65) represent low chemical weathering intensity; values between 65 and 85 indicate moderate chemical weathering, whereas high CIA values (85–100) suggest a strong chemical weathering rate.⁸⁰ Potassium metasomatism alteration may influence CIA values and can be evaluated by the $\text{Al}_2\text{O}_3 - \text{CaO}^* + \text{Na}_2\text{O} - \text{K}_2\text{O}$ (A-CN-K) diagram.⁸¹ All samples from this study were distributed along the ideal weathering trend line predicted by Nesbitt and Young (1984),⁸¹ indicating that the samples are less affected by potassium metasomatism alteration during diagenesis (Figure 9).

CIA values in Stage I vary from 77.4 to 92.1, with an average value of 87.2, reflecting strong chemical weathering under humid and warm conditions. The CIA values from Stage II are between 78.0 and 88.0 ($\bar{x} = 82.9$), indicating a moderate weathering rate under semihumid and warm conditions at this time. In Stage III, CIA values vary from 63.3 to 82.0, with an average value of 74.2 (Figure 7c). Although the average value of 74.2 corresponds to moderate weathering intensity, Stage III represents a relatively low weathering rate under dry and hot conditions when compared to Stages I and II. WIP values show an opposite trend with CIA values, which also suggest a

Table 4. Trace Element Content (ppm) in the Mudstone Samples in the Study Area

sample no.	B	Sc	V	Cr	Co	Ni	Cu	Zn	Ga	Rb	Sr	Y	Mo	Cs	Ba	Th	U	Nb	Ta	Zr	Hf
s1	47.9	15.9	62.6	71.5	62.3	45.4	35.4	122	12.8	141	263	35.5	1.268	11.2	304	15.6	4.67	14.8	1.18	127	0.231
s2	21.1	5.78	86.7	61.7	4.61	27.9	36.7	57.8	12.4	111.4	73	13	2.893	3.81	2.18	15.5	13.23	17.2	1.34	170	4.96
s3	27.4	14.6	83	67.8	5.27	27.2	38.9	63.7	21.6	96.8	69	30.2	3.272	6.99	2.38	15.9	8.38	16.3	1.27	172	4.15
s4	22	12.7	88	63.9	6.18	26.4	40.3	66.6	24.5	94.5	62	34.3	2.966	4.68	2.39	17.3	12.68	15.2	1.31	161	6.1
s5	21.6	16.8	94	70.8	62.9	25.5	42.7	70.8	22.2	102.1	77	31.3	2.886	5.77	2.26	16.1	12.13	14.9	1.25	155	4.39
s6	25	20.1	94	67.6	31.8	25.2	32.1	87	30.4	99.8	69.2	37.2	3.84	2.46	2.37	18.9	10.06	15.7	1.24	137	3
s7	28.3	22.8	103	67.3	60.6	31.2	37.2	62.5	26.1	108.7	53.9	40.4	5.08	11.4	2.48	14.8	12.42	14.6	1.17	224	5.57
s8	27.5	19.3	96.3	65.3	7.76	30.3	33.2	61.8	20.8	109.6	64.3	28.3	7.36	7.14	2.77	18.9	11.37	16.1	1.29	152	3.72
s9	28.6	18.6	102.2	61.7	4.38	28.4	42.4	67.2	21.5	101.2	47.6	31.2	6.97	6.44	2.94	12.1	13.02	15.3	1.32	147	2.25
s10	27.7	4.89	95.4	89.8	7.67	30.7	13.1	15.7	17.74	91.6	42.6	12.7	4.76	6.25	2.17	13.4	11.76	19.5	1.47	148	4.16
s11	34.3	12.8	100.2	77.5	6.39	31.5	37.2	56.7	21.5	104	48.7	29.8	3.98	8.45	2.97	14.7	12.5	22.2	1.81	170	0.424
s12	26.9	14.3	102.2	82.1	13.6	35.2	39.6	71	24.4	111.4	66	24.1	4.61	4.37	2.51	21.1	14.91	22.6	1.84	163	3.79
s13	18.35	13.6	92.8	55.5	6.03	33.9	39	61.6	22	109.6	67	24.4	4.31	8.66	2.30	20.1	8.94	21.3	1.78	166	3.78
s14	17.9	13.1	96	61.9	5.24	28.5	34.5	87.5	22.3	116.2	67	21.5	3.32	7.43	2.72	16.2	9.25	17.1	1.35	184	3.75
s15	19.6	20.3	111	63.4	12.5	31.5	36	89.3	22.4	109.3	72	47	5.11	6.03	3.10	11.6	12.44	18	1.45	164	3.64
s16	23.2	16.1	101	63.7	14.6	31.6	30.4	105	16.5	99.6	67.1	20.6	4.61	4.97	2.39	16.8	9.13	1.23	0.101	186	3.56
s17	22.6	16.8	109	71.8	14.7	32.9	36.6	47.5	28.1	98.6	69	25.3	5.26	9.81	3.02	21.7	7.67	16.4	1.33	186	3.69
s18	18.4	12.2	103.6	77.4	13.5	30.3	43	87	18.3	106	66.3	18.9	5.04	5.51	2.62	21.2	9.75	17.7	1.4	174	5.14
s19	20.9	12.9	98.9	74	9.85	31.4	30.8	98.2	25.3	110.1	65.7	25.8	5.76	6.79	3.08	12.9	12.41	23	1.8	188	5.82
s20	17.6	17	94.8	77.9	9.96	32.5	53	60.1	29.1	94.9	66	28.8	6.68	10.3	2.92	12.3	11.27	14.6	1.23	183	3.35
s21	21.8	10.1	96.1	86.9	6.98	29.8	36.9	107	16.8	127.9	55.4	21.7	4.05	5.28	2.87	10.4	9.18	18.1	1.43	186	2.27
s22	23.1	19.2	90.6	82.3	5.03	30.4	32.7	63.5	33	108.8	57	38.8	4.58	7.88	3.09	16.4	8.25	23	1.84	191	2.68
s23	26.5	15.5	98.7	72.8	8.33	32.37	27.1	53.3	30.9	153	61	47.4	5.32	19.4	3.05	21.6	8.49	21	1.8	190	3.28
s24	25.9	12.2	93.1	98.3	2.03	37.2	30	45.4	20.4	98.1	65.1	20.6	3.71	14.1	3.30	21.4	7.46	17.7	1.49	183	1.57
s25	28.7	11.7	97.6	65.9	8.39	35.3	41.2	108	21.9	95.2	61.2	18.2	2.34	12.3	2.80	14.9	9.8	20	1.64	165	1.18
s26	31.2	13.2	99.9	62.7	5.68	34.9	35.7	82	22.7	95.8	58.6	26.5	2.76	15.3	2.85	13.1	11.03	19.8	1.65	171	3.51
s27	29.8	18.6	53.5	84.1	4.49	36.5	32.6	79	26.9	93	67.1	37.5	0.409	18.5	2.87	21.2	9.6	21.2	1.75	188	4.44
s28	31.4	15.1	52.4	59.8	8.37	38.9	31.3	79	24.3	89	69.2	29.8	0.432	19.1	3.74	22.9	5.98	22.1	1.82	183	3.46
s29	30.5	14.7	57.1	66.3	7.98	36.5	42.3	74	23.6	97	76.8	28.6	0.465	18.2	3.83	24.3	6.52	21.7	1.73	178	4.2
s30	29	15.1	42.4	67.4	17.7	36.3	28.8	114	22.3	92	74	27.9	0.406	20.6	2.75	26.6	5.78	22.5	1.87	172	4.82
s31	28.4	14.8	53.4	69.4	16.9	35.7	31.8	96.2	22.7	91	73.8	30.2	0.578	19.3	2.68	20.7	7.21	20.1	1.81	152	0.409
s32	45.6	16.2	47.9	74.6	20.4	39	118	96	24.1	96.2	64.2	32	0.597	18.1	3.20	19.3	9.54	20.4	1.77	178	3.7
s33	39.1	15.9	58.2	63.1	18.7	36.4	40.3	102	23.8	83	67.2	34.3	0.622	12.6	317	17.4	6.23	20.7	1.77	171	1.6
s34	43.1	16.4	62.8	64.1	14.76	38.8	42.1	88.5	30.2	99.4	62.9	42.9	0.608	26.5	2.70	16.8	5.17	20.8	1.78	169	4.14
s35	34.5	15.4	50.9	64.8	13.2	33.6	35.9	81.3	24.3	96	67.2	36.9	0.614	11.6	2.81	16.9	6.02	22.5	1.82	169	0.523
s36	38.8	14.7	53.3	60.8	18.3	37.4	37.6	85.3	22	86	74.6	35.4	0.597	13.8	3.15	18.7	5.72	21.4	1.69	175	4.65
s37	25.7	13.5	56.5	62.4	16.4	38.6	38.7	97.2	23.1	87	77.3	27.5	0.654	16.7	3.17	19.2	6.12	20.6	1.77	171	4.07
s38	30.2	15.5	58.8	59.9	11.8	37.4	34.1	71	28.8	93	76	50.5	0.7	20.4	3.12	37.7	7.49	22	1.87	164	3.2
s39	39.7	13.5	52.3	61.6	10.1	38.8	37.2	76	20.1	91	87.6	24.8	0.651	8.48	3.14	24.9	4.86	18.9	1.03	146	3.98
s40	36.6	7.95	53.6	66.7	12.55	35.99	36	104	16.2	98	87	14.8	0.88	6.78	3.38	15.7	4.59	14.5	1.38	154	3.1
s41	35.8	7.31	45.1	68.7	5.62	41.53	38.3	91.8	16.9	89.1	78.2	17.2	0.79	5.91	290	17.5	4.76	17.4	1.31	163	3.34
s42	49.9	18.9	99	71.8	19	29.6	41.9	157	13.4	109	373	2.59	17.9	36.8	11.9	15.17	9.5	1.6	101	1.81	4.18
s43	51.2	121	63	13.1	27.8	101	128	13.9	130	319	54.9	2.82	14.8	373	8.5	10.19	15.8	1.41	94	4.18	

Table 4. continued

sample no.	B	Sc	V	Cr	Co	Ni	Cu	Zn	Ga	Rb	Sr	Y	Mo	Cs	Ba	Th	U	Nb	Ta	Zr	Hf
s44	53.7	24.3	172	74	8.91	31.9	112	105	12.9	120	370	40.9	4.26	12.9	467	9.2	14.43	17.6	1.41	80	4.26
s45	47.2	19.7	108.1	71	2.29	36.6	81	111	12.2	117	321	17.1	6.35	0.08	520	8.9	13.91	11.2	0.951	94	4.25
s46	44.2	18.6	117	62.3	24.7	34.8	56.2	156	11.2	122	346	47.4	4.85	17.6	424	9.1	14.19	7.6	0.562	85	3.7
s47	45.9	19	129	68	19.6	35	82.4	155	12.3	133	372	45.1	3.18	15.7	458	10.1	13.21	15.6	1.28	105	3.31
s48	50.4	18.5	99	64.3	62.8	34.7	47.8	64.4	11.5	133	322.3	34.8	5.36	18.3	453	15.4	14.15	16.8	1.31	106	2.53
s49	49.7	17.2	113	69.8	13.6	31.9	46.2	128	13.1	128	313.2	33.6	3.81	17.2	444	10.3	14.23	17.2	1.21	102	2.51
s50	48.9	17.5	110	64.9	15.7	27.3	46.5	132	14.3	121	302	38.2	6.74	16.1	446	10.9	14.73	19.8	1.46	98	3.39
s51	51.4	16.4	89	73.6	16.5	32.5	38.3	144	15.5	131	360	37.9	3.93	16	463	8.6	14.27	17.4	1.35	107	4.97
s52	42.1	15.9	126.2	72.4	15.4	32.8	39.7	123	13.8	131	282.5	28.9	4.84	15.8	428	11.2	14.02	11.7	0.766	91	5.42
s53	49.3	16.9	105.4	75.7	14.6	35.1	36	112	13	121	286.4	32.8	5.85	15.9	403	7.99	10.22	3.23	0.154	79	2.56
s54	45.9	10.32	111.9	61.3	11.7	31.8	42.3	111	12.2	118	294.7	23.7	3.72	13.2	431	11.8	16.02	11.5	0.818	88	2.02
s55	52.3	9.67	112.8	55.7	7.98	29.1	56.1	103.2	14.6	119	263.4	20.7	3.84	8.25	421	12	9.961	18.9	0.951	75.1	4.92
s56	54.5	12.7	64.6	58.4	13.7	44.7	45.6	112	13.3	110	319.1	26.3	0.305	10.2	295	16.7	4.82	17.5	0.98	103	2.81
s57	57.1	14.9	63.6	74.9	16.1	46.1	34.2	101	14.4	113	320	30.4	0.577	12.1	282	17.8	4.93	19.2	1.36	112	3.87

gradual weakening of weathering intensity and further corroborate the interpretation of CIA values (Figure 7d).

5.4. Terrigenous Influx. Elements such as Al, Zr, and Ti are relatively stable in sediments, making them a valid indicator of detrital influx.^{51,82} Al is mainly formed by strong chemical weathering in a warm and humid climate and preserved in clay minerals in fine-grained sediments. In contrast, Zr and Ti are usually transported into ocean sediments as aeolian windblown dust in an arid climate and preserved in heavy minerals such as rutile, zircon, and pyroxene.⁸³ The Al-normalized concentrations of Zr and Ti can therefore be used as terrigenous influx proxies.^{83,84} High Zr/Al and Ti/Al ratios reflect more input of coarse grains and a high deposition rate.⁸⁵

We find that Zr/Al ratios in Stage I vary from 7.37 to 14.88, with an average value of 10.04, indicating a relatively high terrigenous influx (Figure 7e,f). In Stage II, Zr/Al ratios have an average value of 7.66 (6.69–10.07), suggesting moderate terrestrial detrital input during this period. Zr/Al ratios in Stage III are between 4.13 and 7.86 ($\bar{x} = 6.01$), reflecting relatively less input of terrestrial detrital and a low deposition rate. Ti/Al ratios show a similar trend with Zr/Al ratios and have average values of 0.05, 0.04, and 0.03 in Stages I, II, and III, respectively, also suggesting a decreasing terrigenous influx from Stage I to Stage III.

5.5. Redox Conditions. Vanadium can be bound to organic matter by the incorporation of V⁴⁺ into porphyrins and is concentrated in sediments deposited under reducing conditions.^{86,87} Nickel forms soluble Ni²⁺ or NiCl⁺ ions in oxic environments and is removed from sediments into the overlying waters under reducing conditions owing to the absence of sulfides and Mn oxides.⁸⁸ In anoxic environments, vanadium is more effectively fixed in sediments containing organic compounds than nickel. Therefore, V/(V + Ni) ratios have been used to evaluate the oxygenation of the water column, and higher V/(V + Ni) (>0.6) ratios represent more reducing depositional conditions.^{89,90} Mo and U in sedimentary rocks are sensitive to redox conditions and present different enrichment patterns during the sedimentation process.⁵¹ Authigenic U uptake starts at the Fe(II)–Fe(III) redox boundary, whereas authigenic Mo uptake occurs under euxinic conditions in the presence of H₂S.^{91,92} Hence, the U–Mo covariations are widely employed to evaluate paleoredox conditions.^{52,53,93}

Our results show that the V/(V + Ni) ratios have higher values in Stage I (0.71–0.79, $\bar{x} = 0.76$) and Stage III (0.73–0.84, $\bar{x} = 0.78$, Figure 7e), indicating anoxic bottom-water conditions during the deposition of sediments. The lower V/(V + Ni) ratio in Stage II (0.52–0.62, $\bar{x} = 0.58$) suggests that the mudstones in Stage II are deposited under oxic conditions (Figure 7e). The U–Mo pattern shows that the sediments from Stages I and III were deposited under anoxic conditions with strong enrichment of Mo and U. Conversely, Stage II shows less enrichment of Mo and U, reflecting oxic conditions (Figure 10).

5.6. Paleoproductivity. As an essential nutrient for the growth of plankton in aquatic and marine systems, P is closely related to productivity and can be used as an indicator of palaeoproductivity.^{94–96} To eliminate the influence of P from terrigenous debris, the P/Al ratio is often applied to assess changes in paleoproductivity. Ba is characterized by a long residence time in seawater and a high preservation rate and has a close correlation with upwelling and surface productivity, which makes it a suitable indicator for paleo-ocean

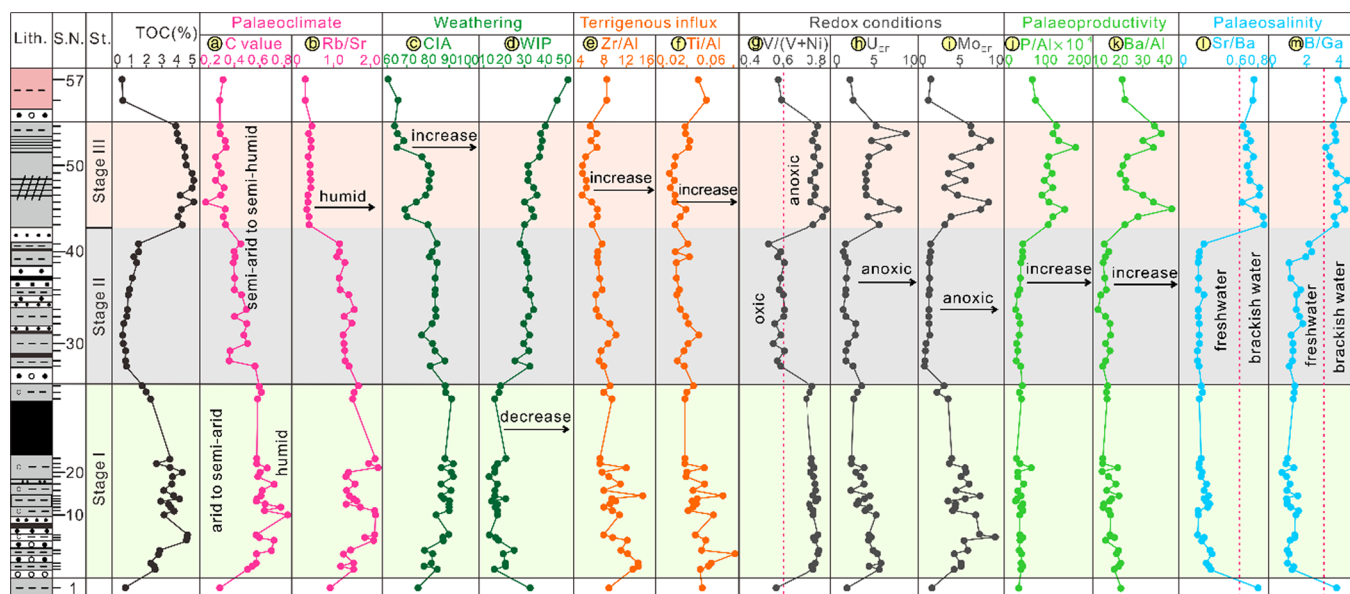


Figure 7. Variation curves of the paleoclimate, weathering, redox conditions, paleoproduction, and paleosalinity proxies of the coal-bearing mudstones of the Dameigou and Shimengou formations. Abbreviations: Litho. – lithology; S.N. – sample number; and St. – Stage.

productivity.^{97,98} Ba/Al ratios are commonly utilized to evaluate paleoproduction levels to eliminate the influence of terrigenous clastic materials.^{99,100} In general, higher P/Al and Ba/Al ratios are indicative of higher paleoproduction levels.

In this study, P/Al ratios show relatively low values in Stage I ($\bar{x} = 34.5 \times 10^{-4}$) and Stage II ($\bar{x} = 29.8 \times 10^{-4}$), and high values in Stage III ($\bar{x} = 116.7 \times 10^{-4}$), reflecting low paleoproduction in Stages I and II, and high paleoproduction during Stage III (Figure 7g). Ba/Al ratios exhibit a similar pattern to the P/Al ratios (Figure 7h), with lower values in Stage I ($\bar{x} = 15.5$) and Stage II ($\bar{x} = 14.1$), and higher values in Stage III ($\bar{x} = 28.5$), implying lower paleoproduction in Stages I and II and higher paleoproduction during Stage III.

5.7. Paleosalinity. The Sr/Ba ratio in sedimentary rocks is often used as a paleosalinity proxy, taking advantage of the different geochemical behaviors of Sr and Ba in sedimentary environments under different water salinities.^{101–103} Sr and Ba occur in soluble carbonates in low-salinity water columns. However, Ba precipitates first in the form of BaSO_4 before Sr with an increase in salinity, leading to higher Sr/Ba ratios in sediments. Generally, Sr/Ba ratios in sediments under saline water conditions are higher than 1, while in freshwater they are lower than 0.6.^{104,105} The TS/TOC ratio has also been applied to indicate salinity related to significant variations in sulfate concentrations in waters with different salinities.¹⁰¹ However, the presence of pyrite in the sedimentary rocks makes TS/TOC ratios a poor paleosalinity indicator since pyrite is the main S-bearing mineral. B is enriched in saline water, and both B and Ga have long residence times in water, which makes the B/Ga ratio a robust salinity indicator in ancient sediments.^{106,107} B/Ga ratios <3 , 3–6, and >6 indicate sediments deposited in freshwater, brackish, and saline conditions, respectively.^{101,108}

In the studied sedimentary succession, Stages I and II show distinctly lower Sr/Ba ratios <0.3 , suggesting that the mudstones in Stages I and II are deposited in freshwater conditions. The Sr/Ba ratios of Stage III vary from 0.62 to 1.01, indicating that the mudstones in Stage III are deposited in a slightly more brackish environment (Figure 7i). B/Ga

ratios exhibit a similar pattern to the Sr/Ba ratios, with lower B/Ga ratios in Stage I (0.60–1.70, $\bar{x} = 1.11$) and Stage II (1.05–2.26, $\bar{x} = 1.53$), indicating freshwater environments. Higher B/Ga ratios in Stage III vary from 3.05 to 4.38 ($\bar{x} = 3.73$), suggesting a brackish water environment (Figure 7j).

5.8. Controlling Factors for Organic Matter Accumulation. Organic matter enrichment in sediments involves a series of complicated physical, chemical, and biological processes and is known to be controlled by multiple factors, including paleosalinity, preservation conditions related to redox conditions, surficial primary productivity, and terrestrial input.^{109–111} These factors are not independent but intricately linked to each other. To probe the factors controlling organic matter accumulation of coal-bearing mudstones from the Middle Jurassic Dameigou and Xiaomeigou formations in the Qaidam Basin, correlation analyses were conducted between the parameters of paleoclimate, weathering degree, terrigenous influx, paleoproduction, redox conditions, paleosalinity, and TOC (Figure 11).

None of the paleoclimate (C values and Rb/Sr ratios), weathering degree (CIA and WIP), terrigenous influx (Zr/Al and Ti/Al ratios), and paleosalinity (Sr/Ba and B/Ga ratios) parameters show clear correlation with TOC in the Dameigou and Shimengou formations, indicating that these factors may not have played an important role in organic matter accumulation (Figure 11a–h). The lack of correlation between paleoproduction proxies (P/Al $\times 10^{-4}$ and Ba/Al ratios), and TOC in Stages I and II may reflect that paleoproduction is not the controlling factor for organic matter accumulation during these intervals (Figure 11i,j). P/Al $\times 10^4$ and Ba/Al ratios and TOC show moderate to strong positive correlations in Stage III, with R^2 values of 0.42 and 0.34, respectively (Figure 11i,j), suggesting that a high paleoproduction level is conducive to organic matter accumulation during Stage III. Both V/(V + Ni) ratios and Mo_{EF} show good positive correlations with TOC in Stages I and II, indicating that redox conditions were important to the preservation and accumulation of organic matter at this time. However, they show poor correlations with the TOC in Stage III, suggesting that the

Table 5. Representative Paleoclimatic and Paleoenvironmental Proxies from the Mudstone Samples in the Study Area

sample no.	C value	Rb/Sr	CIA	WIP	Ti/Al	Zr/Al	V/(V + Ni)	U _{EF}	Mo _{EF}	P/Al (10^{-4})	Ba/Al	Sr/Ba	B/Ga
s1	0.34	0.54	75.21	33.89	0.05	8.30	0.58	1.86	1.66	25.49	19.87	0.87	3.74
s2	0.63	1.53	84.51	17.62	0.05	13.18	0.76	6.25	4.49	33.33	16.90	0.33	1.70
s3	0.62	1.40	77.41	22.05	0.06	14.10	0.75	4.19	5.36	39.34	19.51	0.29	1.27
s4	0.63	1.52	79.57	21.02	0.06	14.12	0.77	6.78	5.20	35.96	20.96	0.26	0.90
s5	0.67	1.33	82.12	20.05	0.06	12.30	0.79	5.87	4.58	36.51	17.94	0.34	0.97
s6	0.73	1.44	77.72	24.46	0.08	11.14	0.79	4.99	6.24	28.46	19.27	0.29	0.82
s7	0.68	2.02	87.76	18.62	0.05	12.24	0.77	4.14	5.55	30.05	13.55	0.22	1.08
s8	0.58	1.70	87.19	16.62	0.06	9.68	0.76	4.42	9.38	42.68	17.64	0.23	1.32
s9	0.58	2.13	89.96	13.84	0.04	7.82	0.78	4.22	7.41	29.79	15.64	0.16	1.33
s10	0.87	2.15	83.13	18.02	0.06	10.88	0.76	5.27	7.00	31.62	15.96	0.20	1.56
s11	0.62	2.14	89.28	17.86	0.04	8.83	0.76	3.96	4.14	44.16	15.43	0.16	1.60
s12	0.76	1.69	90.60	16.02	0.04	8.05	0.74	4.49	4.55	38.50	12.39	0.26	1.10
s13	0.63	1.64	89.40	17.30	0.04	8.69	0.73	2.85	4.51	43.96	12.04	0.29	0.83
s14	0.57	1.73	89.73	14.90	0.04	9.84	0.77	3.02	3.55	19.79	14.55	0.25	0.80
s15	0.57	1.52	87.01	21.36	0.05	8.74	0.78	4.04	5.44	23.97	16.52	0.23	0.88
s16	0.70	1.48	86.12	16.00	0.07	14.88	0.76	4.45	7.38	35.20	19.12	0.28	1.41
s17	0.62	1.43	91.13	16.56	0.04	7.96	0.77	2.00	4.50	26.96	12.92	0.23	0.80
s18	0.70	1.60	86.90	17.11	0.05	11.10	0.77	3.79	6.43	46.56	16.71	0.25	1.01
s19	0.58	1.68	92.14	13.99	0.04	8.45	0.76	3.40	5.18	25.17	13.84	0.21	0.83
s20	0.60	1.44	91.93	16.33	0.04	7.47	0.74	2.80	5.45	26.12	11.92	0.23	0.60
s21	0.65	2.31	87.37	16.60	0.05	12.23	0.76	3.68	5.33	57.86	18.87	0.19	1.30
s22	0.57	1.91	91.74	17.55	0.04	7.37	0.75	1.94	3.53	30.08	11.92	0.18	0.70
s23	0.58	2.51	88.74	21.52	0.04	7.37	0.75	2.01	4.13	23.65	11.83	0.20	0.86
s24	0.58	1.51	91.64	16.07	0.04	8.06	0.71	2.00	3.27	39.21	14.54	0.20	1.27
s25	0.61	1.56	88.76	18.72	0.04	8.05	0.73	2.91	2.28	31.71	13.66	0.22	1.31
s26	0.59	1.63	87.73	19.75	0.04	8.42	0.74	3.31	2.72	40.89	14.04	0.21	1.37
s27	0.50	1.39	81.17	33.81	0.04	8.00	0.59	2.49	0.35	33.18	12.21	0.23	1.11
s28	0.36	1.29	88.04	26.98	0.03	7.23	0.57	1.44	0.34	18.97	14.78	0.19	1.29
s29	0.37	1.26	83.55	32.60	0.04	7.61	0.61	1.70	0.40	24.36	16.37	0.20	1.29
s30	0.47	1.24	82.65	29.47	0.04	8.49	0.54	1.74	0.40	21.21	13.57	0.27	1.30
s31	0.52	1.23	77.99	32.81	0.06	10.07	0.60	2.91	0.77	27.15	17.75	0.28	1.25
s32	0.48	1.50	81.93	29.66	0.04	8.99	0.55	2.94	0.60	36.89	16.17	0.20	1.89
s33	0.46	1.24	83.35	31.79	0.04	7.31	0.62	1.62	0.53	25.21	13.55	0.21	1.64
s34	0.54	1.58	83.13	34.46	0.04	6.69	0.62	1.25	0.48	18.20	10.68	0.23	1.43
s35	0.47	1.43	83.27	32.81	0.03	6.95	0.60	1.51	0.51	23.87	11.56	0.24	1.42
s36	0.44	1.15	83.07	30.62	0.04	7.81	0.59	1.56	0.53	29.46	14.06	0.24	1.76
s37	0.44	1.13	83.09	32.51	0.03	7.25	0.59	1.58	0.55	31.36	13.43	0.24	1.11
s38	0.43	1.22	84.07	31.28	0.03	6.77	0.61	1.89	0.58	35.09	12.88	0.24	1.05
s39	0.42	1.04	81.68	31.87	0.04	6.86	0.57	1.39	0.61	41.84	14.76	0.28	1.98
s40	0.40	1.13	82.60	30.41	0.03	7.11	0.60	1.29	0.81	39.22	15.60	0.26	2.26
s41	0.44	1.14	84.19	28.39	0.04	7.81	0.52	1.39	0.76	40.71	13.89	0.27	2.12
s42	0.30	0.29	80.34	30.87	0.03	6.13	0.77	5.62	3.15	100.18	22.34	1.01	3.72
s43	0.33	0.41	70.70	34.08	0.04	7.14	0.81	4.72	4.29	110.18	28.34	0.86	3.68
s44	0.35	0.32	69.79	33.67	0.04	7.21	0.84	7.93	7.68	141.57	42.11	0.79	4.16
s45	0.19	0.36	74.05	29.91	0.03	6.23	0.75	5.62	8.41	105.96	34.44	0.62	3.87
s46	0.31	0.35	79.69	35.78	0.03	4.13	0.77	4.21	4.72	84.14	20.62	0.82	3.95
s47	0.31	0.36	81.43	33.82	0.03	5.22	0.79	4.00	3.16	113.82	22.76	0.81	3.73
s48	0.27	0.41	80.80	31.43	0.03	5.28	0.74	4.30	5.34	113.55	22.56	0.71	4.38
s49	0.30	0.41	82.01	31.79	0.03	4.79	0.78	4.07	3.58	113.15	20.85	0.71	3.79
s50	0.29	0.40	80.56	31.00	0.03	4.80	0.80	4.40	6.61	100.98	21.86	0.68	3.42
s51	0.26	0.36	77.49	36.31	0.03	5.53	0.73	4.50	4.06	103.36	23.93	0.78	3.32
s52	0.36	0.46	65.53	38.21	0.04	7.40	0.79	6.95	7.87	169.92	34.80	0.66	3.05
s53	0.34	0.42	68.03	38.85	0.04	6.03	0.75	4.76	8.93	134.35	30.76	0.71	3.79
s54	0.30	0.40	64.98	37.16	0.04	7.86	0.78	8.72	6.64	119.64	38.48	0.68	3.76
s55	0.30	0.45	63.28	40.17	0.04	6.39	0.79	5.16	6.53	122.45	35.80	0.63	3.58
s56	0.30	0.34	65.35	46.96	0.06	8.51	0.59	2.43	0.50	70.25	24.38	1.08	4.10
s57	0.34	0.35	60.25	51.66	0.05	8.42	0.58	2.26	0.87	61.65	21.20	1.13	3.97

redox condition is not the major controlling factor for organic matter accumulation during Stage III.

5.9. Organic Matter Accumulation Model. Based on the correlation analysis above, it can be inferred that the

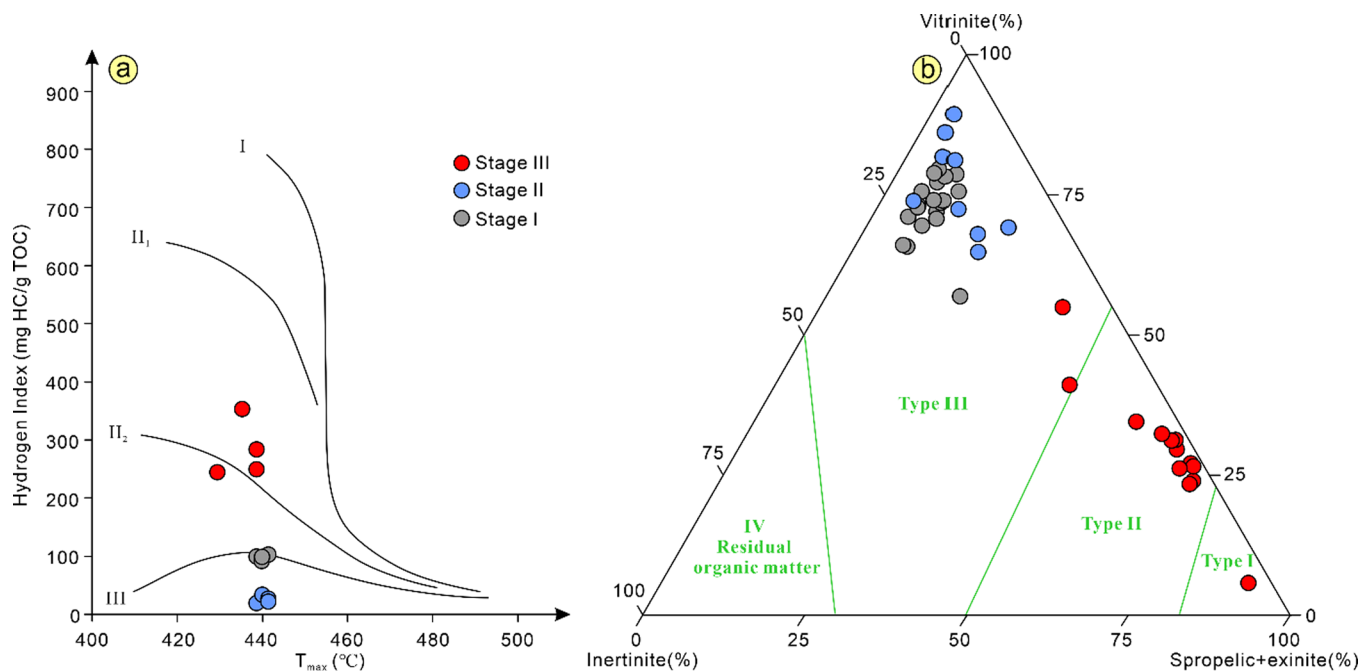


Figure 8. Types of organic matter in coal-bearing mudstones of the Dameigou and Shimengou formations. (a) Cross plot of HI and T_{max} ; (b) triangle diagram of microcomponents vitrinite, inertinite, and spropellic + exinite.

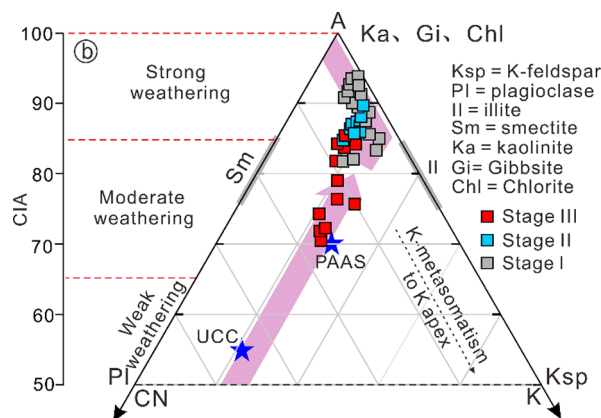


Figure 9. A-CN-K ($\text{Al}_2\text{O}_3 - (\text{CaO}^* + \text{Na}_2\text{O}) - \text{K}_2\text{O}$) diagram for the mudstone samples from the Dameigou and Shimengou formations with the chemical index of alteration (CIA) scale to the left.

accumulation of organic matter in Stages I and II was primarily controlled by redox conditions, while paleoproductivity is the major controlling factor for organic matter accumulation in Stage III. Combined with the analysis of organic matter sources, here we develop a model that illustrates the mechanisms of organic matter accumulation of the coal-bearing mudstones in the Middle Jurassic Dameigou and Shimengou formations (Figure 12).

During the deposition of sediments in Stage I, a warm and humid climate prevailed in the study area, indicated by higher C values and Rb/Sr ratios, leading to the large-scale growth of terrestrial higher plants (Figure 12a). Concurrently, enhanced precipitation contributed to the intensification of surface runoff and acceleration of the chemical weathering rate evidenced by high CIA values and low WIP values, promoting the transport of abundant terrigenous detrital to the lake as indicated by high Zr/Al and Ti/Al ratios (Figure 12a). It is worth noting that abundant terrigenous detrital transported into the lake did not

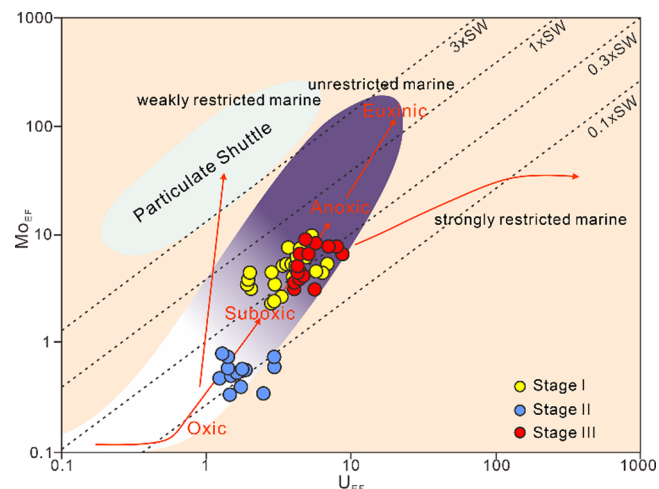


Figure 10. Covariation plot of U_{EF} and Mo_{EF} for the mudstone samples from the Dameigou and Shimengou formations.

contribute to an increase in paleoproductivity, implied by low P/Al and Ba/Al ratios. This may be attributed to the relatively low nutrient concentrations (such as Cu and Zn) in the parent rock (Table 4).

Abundant terrestrial higher plant debris delivered in terrigenous detrital provided abundant organic matter sources, leading to the development of type III kerogen in mudstones deposited during Stage I. Concurrently, a larger sinking flux of organic matter intensifies respiratory oxygen consumption in water columns,^{112,113} resulting in the establishment of anoxic bottom-water conditions implied by higher $\text{V}/(\text{V} + \text{Ni})$ ratios and the strong enrichment of Mo and U. Anoxic bottom-water conditions further promoted the preservation of organic matter, contributing to the relatively high contents of TOC in the mudstones of Stage I (Figure 12a).

During the deposition of Stage II, as the humidity decreased, a semihumid and warm climate prevailed in the study area

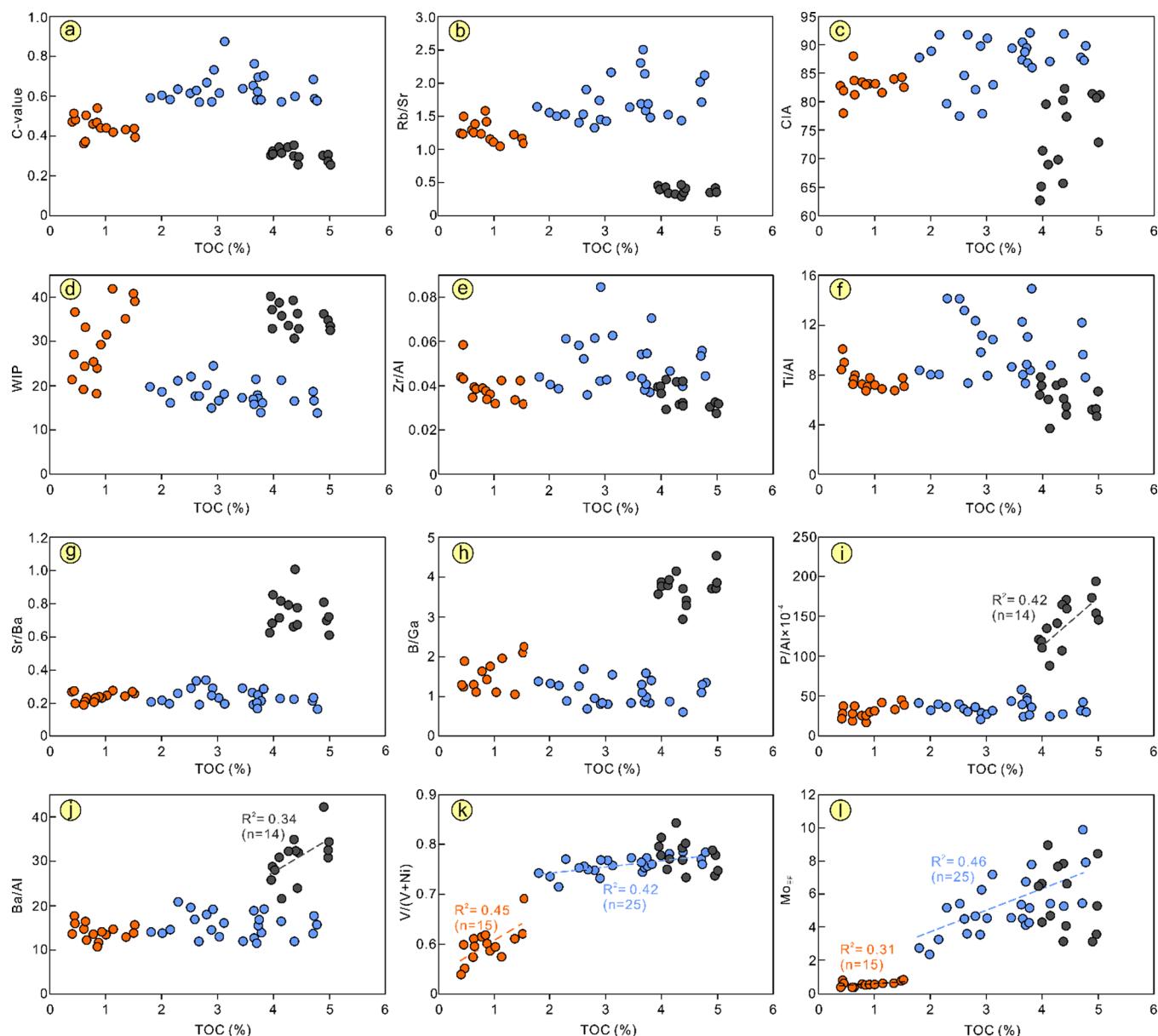


Figure 11. Correlations between TOC content and proxies of paleoclimate, weathering trends, terrigenous influx, paleosalinity, primary productivity, and paleoredox conditions for mudstone samples from the Dameigou and Shimengou formations. (a) TOC versus (vs) C value; (b) TOC vs Rb/Sr; (c) TOC vs CIA; (d) TOC vs WIP; (e) TOC vs Zr/Al; (f) TOC vs Ti/Al; (g) TOC vs Sr/Ba; (h) TOC vs B/Ga; (i) TOC vs P/Al $\times 10^{-4}$; (j) TOC vs Ba/Al; (k) TOC vs V/(V + Ni); and (l) TOC vs Mo_{EF}.

(Figure 12b), evidenced by paleoclimate indicators (C values and Rb/Sr ratios) during Stage II compared to Stage I. Decreased precipitation weakened surface runoff and chemical weathering implied by CIA and WIP values, which further contributed to the decrease of terrigenous detrital input into the lake suggested by the decrease of Zr/Al and Ti/Al ratios. This led to a decreased sinking flux of organic carbon and a decrease in the consumption of dissolved oxygen in the lake water, resulting in a transition from anoxic to oxic bottom-water conditions indicated by the decrease of V/(V + Ni) ratios and less enrichment of Mo and U (Figure 12b). In addition, the paleoproductivity was low, evidenced by low P/Al ratios and Ba/Al ratios, which made terrestrial higher plants the predominant organic matter source at the time, forming type III kerogen in Stage II mudstones. Overall, the poor preservation of organic matter and insufficient organic matter

sources in the lake contributed to the lower TOC contents of Stage II mudstones (Figure 12b).

During the deposition of sediments in Stage III, a dry and hot climate prevailed in the study area, indicated by lower C values and Rb/Sr ratios, which reduced surface runoff and weakened chemical weathering implied by lower CIA values and higher WIP values, resulting in low terrigenous detrital input evidenced by low Zr/Al and Ti/Al ratios (Figure 12c). Due to the intensification of water evaporation and the decrease in freshwater supply, authigenic minerals such as calcite, dolomite, and aragonite dominated during the deposition in Stage III (Figure 5) and the salinity of the previous freshwater lake increased gradually, as evidenced by the increase of Sr/Ba and B/G ratios. The high salinity promoted the stratification of the water column. Although increased salinity may have decreased biological diversity to

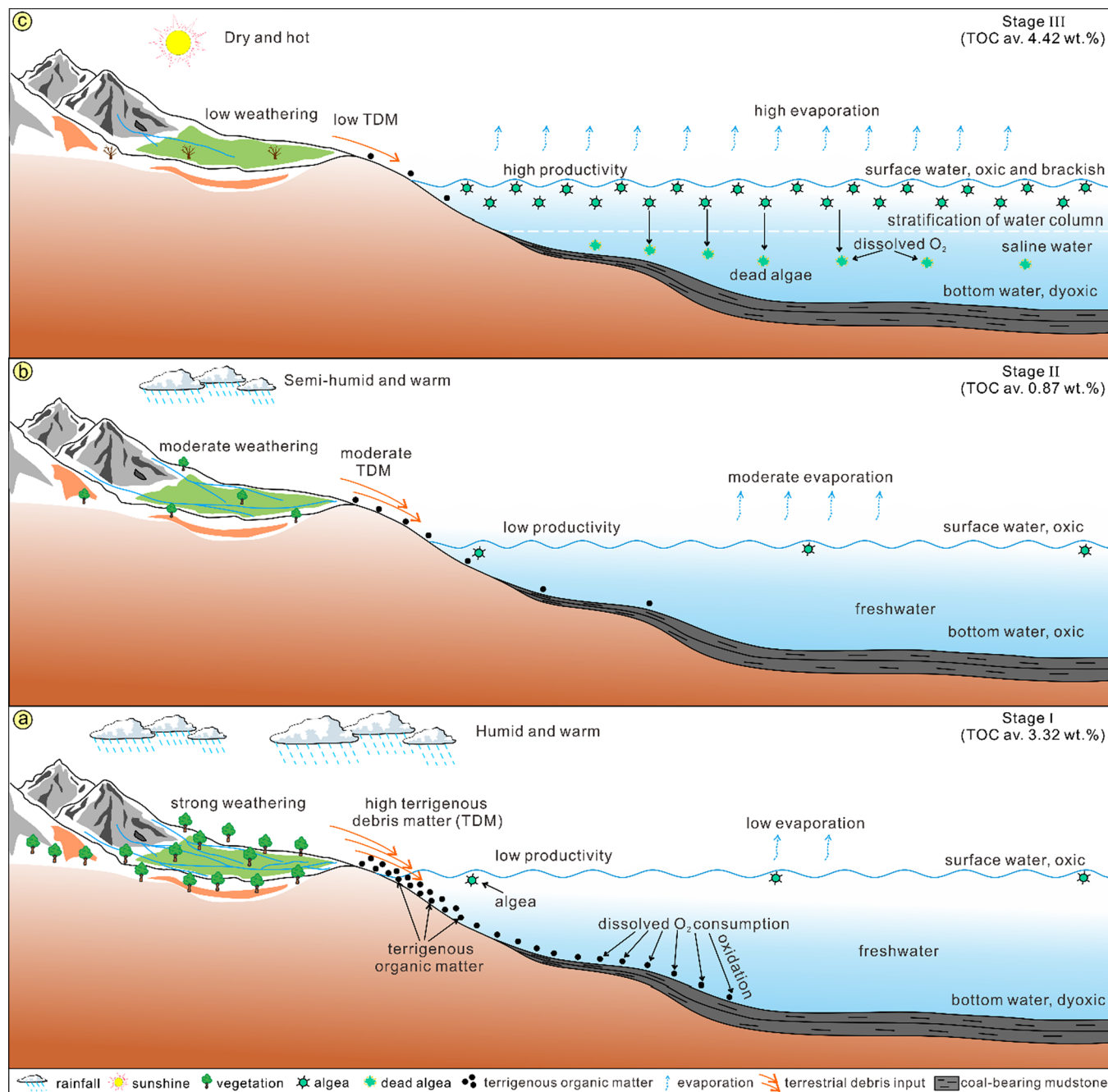


Figure 12. Cartoon showing the organic matter accumulation models of coal-bearing mudstones in the Dameigou and Shimengou formations. (a) Stage I; (b) Stage II; and (c) Stage III.

some extent, it is conducive to halotolerant plankton,¹¹⁴ leading to surface water's high primary productivity, indicated by higher P/Al and Ba/Al ratios (Figure 12c). Thus, a small portion of terrestrial higher plants and a large portion of lower aquatic organisms constitute a mixed organic matter source, leading to the development of type II kerogen in mudstones that deposited during Stage III. Meanwhile, dissolved oxygen in the lake water was rapidly consumed by the subsequent decomposition of dead algae, resulting in anoxic bottom-water conditions, indicated by redox proxies ($V/(V + Ni)$) and enrichment factors of Mo and U) and the occurrence of pyrite (Figure 12). High primary productivity and anoxic bottom-water conditions were conducive to the formation and

preservation of organic matter, contributing to the higher TOC contents in Stage III mudstones (Figure 12c).

Overall, unlike previous studies that only focused on the latest Middle Jurassic organic-rich shale, we present high-resolution geochemical characterization for the entire Middle Jurassic coal-bearing mudstones and reconstruct the paleoclimatic and paleoenvironmental conditions in the Qaidam Basin during the Middle Jurassic. Our findings support the view that a high surficial primary productivity is the main reason for organic matter enrichment of the mudstones in the latest Middle Jurassic (Callovian), proposed by previous studies concerning the Yuqia and Tuanyushan area. Meanwhile, we also found that the mudstones in the early to late Middle Jurassic (Aalenian to Bathonian) have relatively low

surficial primary productivity, and bottom-water redox conditions are the major controlling factors for organic matter accumulation during these intervals.

6. CONCLUSIONS

- (1) Three significant depositional stages, with average TOC values of 3.32% (Stage I), 0.87% (Stage II), and 4.42% (Stage III), are recognized from the bottom to the top in the Middle Jurassic Dameigou and Shimengou formations from the Qaidam Basin.
- (2) Stage I was deposited in a warm and humid climate, corresponding to strong weathering, low paleoproducitivity, freshwater, and anoxic bottom-water conditions. Stage II was developed in a paleoenvironmental condition of moderate weathering rate, low paleoproducitivity, freshwater, and oxic bottom water, and in a semihumid and warm climate. Stage III was deposited in a dry and hot climate, leading to relatively low weathering intensity, a high paleoproducitivity level, and brackish and anoxic bottom-water conditions.
- (3) Paleoproducitivity and redox conditions are two major factors controlling organic matter accumulation in the Middle Jurassic Dameigou and Shimengou formations. The accumulation of organic matter in Stages I and II was primarily controlled by redox conditions, while paleoproducitivity is the major controlling factor for organic matter accumulation in Stage III.
- (4) We present high-resolution geochemical characterization and suggest a model that illustrates the mechanisms of organic matter accumulation for the entire Middle Jurassic coal-bearing mudstones, which provides a better understanding of the depositional process and driving mechanisms for organic matter accumulation in the Middle Jurassic Dameigou and Shimengou formations.

AUTHOR INFORMATION

Corresponding Author

Jing Lu – State Key Laboratory of Coal Resources and Safe Mining, and College of Geoscience and Surveying Engineering, China University of Mining and Technology, Beijing 100083, China; Email: lujing@cumtb.edu.cn

Authors

Kai Zhou – State Key Laboratory of Hydroscience and Engineering, Department of Hydraulic Engineering, Tsinghua University, Beijing 100084, China; State Key Laboratory of Coal Resources and Safe Mining, and College of Geoscience and Surveying Engineering, China University of Mining and Technology, Beijing 100083, China; orcid.org/0000-0002-6562-694X

Jinyan Sun – Gansu Water Conservancy & Hydro Power Survey & Design Research Institute, Jiayuguan, Gansu 730099, China

Minfang Yang – Research Institute of Petroleum Exploration and Development, PetroChina, Beijing 100083, China

Shuo Zhang – State Key Laboratory of Hydroscience and Engineering, Department of Hydraulic Engineering, Tsinghua University, Beijing 100084, China

Weichao Wang – Qinghai Bureau of Coal Geology, China National Administration of Coal Geology, Xining 810001, China

Ran Gao – SINOPEC Exploration & Production Research Institute, Beijing 100083, China

Peixin Zhang – School of Municipal and Environmental Engineering, Henan University of Urban Construction, Pingdingshan 467036 Henan, China

Wanqing Wang – State Key Laboratory of Coal Resources and Safe Mining, and College of Geoscience and Surveying Engineering, China University of Mining and Technology, Beijing 100083, China

Haoqing Liu – State Key Laboratory of Coal Resources and Safe Mining, and College of Geoscience and Surveying Engineering, China University of Mining and Technology, Beijing 100083, China

Longyi Shao – State Key Laboratory of Coal Resources and Safe Mining, and College of Geoscience and Surveying Engineering, China University of Mining and Technology, Beijing 100083, China; orcid.org/0000-0001-9975-6091

Complete contact information is available at:
<https://pubs.acs.org/10.1021/acsomega.3c05433>

Notes

The authors declare no competing financial interest.

ACKNOWLEDGMENTS

The authors express their great thanks to the “No. 105 Exploration Team, Qinghai Bureau of Coal Geology” for support with borehole data. This research was supported by the National Natural Science Foundation of China (Grants 42302191, 42172196, 41772161, and 41472131), and the Research on CBM Exploration and Development Technology, Topic 3 of the “New Bedding System and New Field Strategy and Evaluation Technology for New CBM Regions” (2021DJ2303).

REFERENCES

- (1) Fleet, A. J.; Scott, A. C. Coal and coal-bearing strata as oil-prone source rocks: an overview. *Geol. Soc. Spec. Publ.* **1994**, *77*, 1–8.
- (2) Li, M.; Bao, J.; Lin, R.; Stasiuk, L. D.; Yuan, M. Revised models for hydrocarbon generation, migration and accumulation in Jurassic coal measures of the Turpan basin, NW China. *Org. Geochem.* **2001**, *32*, 1127–1151.
- (3) Sun, P. C.; Chsenhofer, R. F.; Liu, Z. J.; Strobl, S. A. I.; Meng, Q. T.; Liu, R.; Zhen, Z. Organic matter accumulation in the oil shale and coal-bearing Huadian Basin (Eocene; NE China). *Int. J. Coal Geol.* **2013**, *105*, 1–15.
- (4) Li, Y.; Tang, D.; Wu, P.; Niu, X.; Wang, K.; Qiao, P.; Wang, Z. Continuous unconventional natural gas accumulations of Carboniferous-Permian coal-bearing strata in the Linxing area, northeastern Ordos basin. *China. J. Nat. Gas Sci. Eng.* **2016**, *36*, 314–327.
- (5) Qian, Y.; Zhang, T.; Wang, Z.; Tuo, J.; Zhang, M.; Wu, C.; Tian, C. Organic geochemical characteristics and generating potential of source rocks from the Lower-Middle Jurassic coal-bearing strata in the East Junggar Basin, NW China. *Mar. Petrol. Geol.* **2018**, *93*, 113–126.
- (6) Quan, Y.; Chen, Z.; Jiang, Y.; Diao, H.; Xie, X.; Lu, Y.; Du, X.; Liu, X. Hydrocarbon generation potential, geochemical characteristics, and accumulation contribution of coal-bearing source rocks in the Xihu Sag, East China Sea Shelf Basin. *Mar. Petrol. Geol.* **2022**, *136*, No. 105465.
- (7) Yu, K.; Ju, Y.; Wan, Z.; Zhao, K. Paleoenvironment, provenance, and hydrocarbon potential of lower Permian coal-bearing source rocks in the southern north China basin: A case study of the Pingdingshan coalfield. *ACS Earth Space Chem.* **2022**, *6*, 1299–1310.
- (8) Hendrix, M. S.; Brassell, S. C.; Carroll, A. R.; Graham, S. A. Sedimentology, organic geochemistry, and petroleum potential of

- Jurassic coal measures: Tarim, Junggar, and Turpan basins, northwest China. *AAPG Bull.* **1995**, *79*, 929–958.
- (9) Wang, D. D.; Shao, L. Y.; Li, Z. X.; Li, M. P.; Lv, D.; Liu, H. Hydrocarbon generation characteristics, reserving performance and preservation conditions of continental coal measure shale gas: A case study of Mid-Jurassic shale gas in the Yan'an Formation, Ordos Basin. *J. Petrol. Sci. Eng.* **2016**, *145*, 609–628.
- (10) Wu, C.; Zhang, M.; Xiong, D.; Tuo, J.; Ma, W.; Qian, Y. Gas generation from Jurassic coal measures at a low mature stage and potential gas accumulation in the eastern Junggar Basin, China. *J. Nat. Gas Sci. Eng.* **2022**, *84*, No. 103692.
- (11) Guo, Z.; Xie, Z.; Li, J.; Tian, J.; Zeng, X.; Ma, W. Resource potential of the Jurassic gas system, northern margin of the Qaidam Basin, northwestern China. *AAPG Bull.* **2021**, *105*, 883–917.
- (12) Wan, J.; Huang, W.; Gong, Y.; Zhuo, Q.; Lu, X. Hydrocarbon Accumulation Process and Mechanism in the Lower Jurassic Reservoir in the Eastern Kuqa Depression, Tarim Basin, Northwest China: A Case Study of Well Tudong 2 in the Tugerming Area. *ACS omega* **2021**, *6* (45), 30344–30361.
- (13) Anderson, R. Y.; Dean, W. E. Lacustrine varve formation through time. *Palaeogeogr. Palaeoclimatol. Palaeoecol.* **1988**, *62*, 215–235.
- (14) Chamberlain, C. P.; Wan, X.; Graham, S. A.; Carroll, A. R.; Doeberl, A. C.; Sageman, B. B.; Peter, B.; Malinda, L. K.; Zhou, W.; Wang, C. S. Stable isotopic evidence for climate and basin evolution of the Late Cretaceous Songliao basin, China. *Palaeogeogr., Palaeoclimatol. Palaeoecol.* **2013**, *385*, 106–124.
- (15) Wang, M.; Wilkins, R. W.; Song, G.; Zhang, L.; Xu, X.; Li, Z.; Chen, G. Geochemical and geological characteristics of the Es3 L lacustrine shale in the Bonan sag, Bohai Bay Basin, China. *Int. J. Coal Geol.* **2015**, *138*, 16–29.
- (16) Lu, J.; Zhou, K.; Yang, M. F.; Zhang, P. X.; Shao, L. Y.; Hilton, J. Records of organic carbon isotopic composition ($\delta^{13}\text{C}_{\text{org}}$) and volcanism linked to changes in atmospheric pCO_2 and climate during the Late Paleozoic Icehouse. *Glob. Planet. Chang.* **2021**, *207*, No. 103654.
- (17) Bai, Y.; Liu, Z.; Sun, P.; Liu, R.; Hu, X.; Zhao, H.; Xu, Y. Rare earth and major element geochemistry of Eocene fine-grained sediments in oil shale-and coal-bearing layers of the Meihe Basin, Northeast China. *J. Asian Earth Sci.* **2015**, *97*, 89–101.
- (18) Cheng, X.; Hou, D.; Zhou, X.; Liu, J.; Diao, H.; Jiang, Y.; Yu, Z. Organic geochemistry and kinetics for natural gas generation from mudstone and coal in the Xihu Sag, East China Sea Shelf Basin, China. *Mar. Petrol. Geol.* **2020**, *118*, No. 104405.
- (19) Wang, Q.; Liu, W.; Meng, P.; Hu, J.; Wang, X.; Zhang, D.; Liu, J. Assessment the gas potential of coal-bearing mudstones from upper paleozoic basin via gold-tube pyrolysis. *J. Nat. Gas Sci. Eng.* **2021**, *90*, No. 103895.
- (20) Dai, J. X.; Wang, T. B.; Song, Y. *Forming Conditions and Distributions of Large Middle Natural Gas Fields in China*; Geological Publishing House: Beijing 1997; pp 1–237 (in Chinese).
- (21) Ritts, B. D.; Hanson, A. D.; Zinniker, D.; Moldowan, J. M. Lower–Middle Jurassic nonmarine source rocks and petroleum systems of the northern Qaidam basin, northwest China. *AAPG Bull.* **1999**, *83*, 1980–2005.
- (22) Shao, L. Y.; Li, M.; Li, Y. H.; Zhang, Y. P.; Lu, J.; Zhang, W. L.; Tian, Z.; Wen, H. J. Geological characteristics and controlling factors of shale gas in Jurassic of northern Qaidam Basin. *Earth Sci. Front.* **2014**, *21*, 311–322. (In Chinese)
- (23) Hou, H.; Shao, L.; Li, Y.; Liu, L.; Liang, G.; Zhang, W.; Wang, X.; Wang, W. Effect of paleoclimate and paleoenvironment on organic matter accumulation in lacustrine shale: Constraints from lithofacies and element geochemistry in the northern Qaidam Basin, NW China. *J. Petrol. Sci. Eng.* **2022**, *208*, No. 109350.
- (24) Yang, Y.; Zhang, B.; Zhao, C.; Xu, T. Mesozoic source rocks and petroleum systems of the northeastern Qaidam basin, northwest China. *AAPG Bull.* **2004**, *88*, 115–125.
- (25) Zhang, H.; Li, H.; Xiong, C.; Zhang, H.; Wang, Y.; He, Z.; Lin, G.; Sun, B. Jurassic coal-bearing strata and coal accumulation in Northwest China; Geological Publishing House: Beijing, 1998; pp 1–317 (in Chinese).
- (26) Wang, Y.; Mosbrugger, V.; Zhang, H. Early to Middle Jurassic vegetation and climatic events in the Qaidam Basin, Northwest China. *Palaeogeogr. Palaeoclimatol. Palaeoecol.* **2005**, *224*, 200–216.
- (27) Zhang, P.; Yang, M.; Lu, J.; Jiang, Z.; Zhou, K.; Liu, H.; He, Z.; Wang, Y.; Bian, X.; Shao, L.; Hilton, J.; Bond, D. P. Middle Jurassic terrestrial environmental and floral changes linked to volcanism: Evidence from the Qinghai-Tibet Plateau, China. *Glob. Planet. Chang.* **2023**, *223*, No. 104094.
- (28) Huang, G. W.; Pan, J. Y.; Xia, F.; Yan, J.; Zhang, C. Y.; Wu, D. H.; Liu, Y. Provenance of uranium mineralization of the Yuqia area, Northwest China: Constraints from detrital zircon U-Pb geochronology and Hf isotopes. *J. Earth Sci.* **2022**, *33*, 1549–1570.
- (29) Yu, L.; Xiao, A.; Wu, L.; Tian, Y.; Rittner, M.; Lou, Q.; Pan, X. Provenance evolution of the Jurassic northern Qaidam Basin (West China) and its geological implications: evidence from detrital zircon geochronology. *Int. J. Earth Sci.* **2017**, *106*, 2713–2726.
- (30) Lu, J.; Zhou, K.; Yang, M. F.; Shao, L. Y. Jurassic continental coal accumulation linked to changes in palaeoclimate and tectonics in a fault-depression superimposed basin, Qaidam Basin, NW China. *Geol. J.* **2020**, *55*, 7998–8016.
- (31) Zhou, K.; Wang, W.; Yang, M.; Gao, R.; Liu, H.; Shao, L.; Lu, J. Evolution of depositional environment of the Pliensbachian Stage (Lower Jurassic) coal-bearing series in the Qaidam Basin, NW China. *Geol. J.* **2023**, *58*, 3948.
- (32) Lu, J.; Shao, L. Y.; Yang, M. F.; Zhou, K.; Wheeley, J. R.; Wang, H.; Hilton, J. Depositional model for peat swamp and coal facies evolution using sedimentology, coal macerals, geochemistry, and sequence stratigraphy. *J. Earth Sci.* **2017**, *28*, 1163–1177.
- (33) Hou, H.; Shao, L.; Li, Y.; Li, Z.; Zhang, W.; Wen, H. The pore structure and fractal characteristics of shales with low thermal maturity from the Yuqia Coalfield, northern Qaidam Basin, northwestern China. *Front. Earth Sci.* **2018**, *12*, 148–159.
- (34) Hou, H.; Shao, L.; Li, Y.; Li, Z.; Wang, S.; Zhang, W.; Wang, X. Influence of coal petrology on methane adsorption capacity of the Middle Jurassic coal in the Yuqia Coalfield, northern Qaidam Basin, China. *J. Petrol. Sci. Eng.* **2017**, *149*, 218–227.
- (35) Guo, T.; Ren, S.; Luo, X.; Bao, S.; Wang, S.; Zhou, Z.; Chen, X.; Li, H.; Xu, Q. Accumulation conditions and prospective areas of shale gas in the Middle Jurassic Dameigou Formation, northern Qaidam Basin, Northwest China. *Geol. J.* **2018**, *53*, 2944–2954.
- (36) Liu, S.; Tang, S.; Tan, F.; Zhao, C.; Li, Y.; Wang, S.; Huo, T. Pore structure characteristics and hydrocarbon generation potential of middle Jurassic lacustrine source rocks in the Yuka depression, Qaidam Basin, NW China: Implications from petrographic and organic geochemical analyses. *J. Nat. Gas Sci. Eng.* **2020**, *81*, No. 103481.
- (37) Wang, Y.; Xu, S.; Hao, F.; Poulton, S. W.; Zhang, Y.; Guo, T.; Lu, Y. B.; Bai, N. Arid climate disturbance and the development of salinized lacustrine oil shale in the Middle Jurassic Dameigou Formation, Qaidam Basin, northwestern China. *Palaeogeogr., Palaeoclimatol., Palaeoecol.* **2021**, *577*, No. 110533.
- (38) Xie, W.; Tan, J.; Wang, W.; Schulz, H. M.; Liu, Z.; Kang, X.; Wang, Y.; Shahzad, A.; Jan, I. U. Middle Jurassic lacustrine source rocks controlled by an aridification event: A case study in the northern Qaidam Basin (NW China). *Int. J. Coal Geol.* **2021**, *242*, No. 103779.
- (39) Wu, Z.; Grohmann, S.; Littke, R.; Guo, T.; He, S.; Baniasad, A. Organic petrologic and geochemical characterization of petroleum source rocks in the Middle Jurassic Dameigou Formation, Qaidam Basin, northwestern China: Insights into paleo-depositional environment and organic matter accumulation. *Int. J. Coal Geol.* **2022**, *259*, No. 104038.
- (40) Jian, X.; Guan, P.; Zhang, W.; Feng, F. Geochemistry of Mesozoic and Cenozoic sediments in the northern Qaidam basin, northeastern Tibetan Plateau: implications for provenance and weathering. *Chem. Geol.* **2013**, *360*, 74–88.

- (41) Sun, H. S.; Li, H.; Algeo, T. J.; Gabo-Ratio, J. A. S.; Yang, H.; Wu, J. H.; Wu, P. Geochronology and geochemistry of volcanic rocks from the Tanjianshan Group, NW China: Implications for the early Paleozoic tectonic evolution of the North Qaidam Orogen. *Geol. J.* **2019**, *54*, 1769–1796.
- (42) Sun, H.; Li, H.; Evans, N. J.; Yang, H.; Wu, P. Volcanism, mineralization and metamorphism at the Xitieshan Pb–Zn deposit, NW China: Insights from zircon geochronology and geochemistry. *Ore Geol. Rev.* **2017**, *88*, 289–303.
- (43) Li, J. H.; Jiang, H. F. *Global Ancient Plate Reconstruction, Lithofacies Paleogeography and Ancient Environment Atlas*; Geological Publishing House: Beijing, 2013; pp 1–123 (in Chinese).
- (44) Wei, B. An analysis on tectonic paleogeography of the Qaidam Basin, NW China. *Earth Sci. Front.* **2000**, *7*, 421–429. (In Chinese)
- (45) Liu, T. J.; Shao, L. Y.; Cao, D. Y.; Ju, Q.; Guo, J. N.; Lu, J. *Jurassic coal resources Formation conditions and resource evaluation in the northern margin of Qaidam Basin*; Geological Publishing House: Beijing, 2013; pp 1–276 (in Chinese).
- (46) Yang, Y.; Guo, Z.; Luo, Y. Middle-Late Jurassic tectonostratigraphic evolution of Central Asia, implications for the collision of the Karakoram-Lhasa Block with Asia. *Earth-Sci. Rev.* **2017**, *166*, 83–110.
- (47) Cao, Q. Y. Identification of microcomponents and types of kerogen under transmitted light. *Pet. Explor. Dev.* **1985**, *5*, 14–23. (In Chinese)
- (48) Nesbitt, H. W.; Young, G. M. Early Proterozoic climates and plate motions inferred from major element chemistry of lutites. *Nature* **1982**, *299*, 715–717.
- (49) Parker, A. An index of weathering for silicate rocks. *Geol. Mag.* **1970**, *107*, 501–504.
- (50) Zhao, Z. Y.; Zhao, J. H.; Wang, H. J.; Liao, J. D.; Liu, C. M. Distribution characteristics and applications of trace elements in Junggar Basin. *Nat. Gas Explor. Dev.* **2007**, *30*, 30–33. (In Chinese)
- (51) McLennan, S. M. Weathering and global denudation. *J. Geol.* **1993**, *101*, 295–303.
- (52) Tribouillard, N.; Algeo, T. J.; Lyons, T.; Riboulleau, A. Trace metals as paleoredox and paleoproductivity proxies: an update. *Chem. Geol.* **2006**, *232*, 12–32.
- (53) Algeo, T. J.; Li, C. Redox classification and calibration of redox thresholds in sedimentary systems. *Geochim. Cosmochim. Acta* **2020**, *287*, 8–26.
- (54) Taylor, S. R.; McLennan, S. M. *The Continental Crust: Its Composition and Evolution*; Blackwell: Oxford, 1985; pp 1–312.
- (55) Meyers, P. A.; Ishiwatari, R. Lacustrine organic geochemistry—an overview of indicators of organic matter sources and diagenesis in lake sediments. *Org. geochem.* **1993**, *20*, 867–900.
- (56) Moldowan, J. M.; Seifert, W. K.; Gallegos, E. J. Relationship between petroleum composition and depositional environment of petroleum source rocks. *AAPG Bull.* **1985**, *69*, 1255–1268.
- (57) Mao, J.; Fang, X.; Lan, Y.; Schimmelmann, A.; Mastalerz, M.; Xu, L.; Schmidt-Rohr, K. Chemical and nanometer-scale structure of kerogen and its change during thermal maturation investigated by advanced solid-state ^{13}C NMR spectroscopy. *Geochim. Cosmochim. Acta* **2010**, *74*, 2110–2127.
- (58) Stahl, W. J.; Wollanke, G.; Boigk, H. Carbon and nitrogen isotope data of Upper Carboniferous and Rotliegend natural gases from North Germany and their relationship to the maturity of the organic source material. In *Proceedings of the 7th International Meeting on Organic Geochemistry Advances in Organic Geochemistry*, 1975; Madrid; pp 539–560.
- (59) Bordenave, M. L.; Espitalié, J.; Leplat, P. O. J. L.; Oudin, J. L.; Vandebroucke, M. Screening techniques for source rock evaluation. In Bordenave, M. L. (Ed.), *Applied Petroleum Geochemistry*; Editions Technip: Paris, 1993; pp 218–278.
- (60) Miao, H.; Wang, Y.; Zhao, S.; Guo, J.; Ni, X.; Gong, X.; Zhang, Y.; Li, J. Geochemistry and organic petrology of middle Permian source rocks in Taibei Sag, Turpan-Hami Basin, China: Implication for organic matter enrichment. *ACS omega* **2021**, *6*, 31578–31594.
- (61) Cai, C.; Xiang, L.; Yuan, Y.; Xu, C.; He, W.; Tang, Y.; Borjigin, T. Sulfur and carbon isotopic compositions of the Permian to Triassic TSR and non-TSR altered solid bitumen and its parent source rock in NE Sichuan Basin. *Org. Geochem.* **2017**, *105*, 1–12.
- (62) He, S.; Qin, Q.; Li, H.; Zhao, S. Geological characteristics of deep shale gas in the Silurian Longmaxi Formation in the southern Sichuan Basin, China. *Front. Earth Sci.* **2022**, *9*, No. 818155.
- (63) Cao, J.; Wu, M.; Chen, Y.; Hu, K.; Bian, L. Z.; Wang, L. C.; Zhang, Y. Trace and rare earth element geochemistry of Jurassic mudstones in the northern Qaidam Basin, northwest China. *Geochemistry* **2012**, *72*, 245–252.
- (64) Zhou, K.; Lu, J.; Zhang, S.; Yang, M.; Gao, R.; Shao, L.; Hilton, J. Volcanism driven Pliensbachian (Lower Jurassic) terrestrial climate and environment perturbations. *Glob. Planet. Chang.* **2022**, *216*, No. 103919.
- (65) Fathy, D.; Wagreich, M.; Gier, S.; Mohamed, R. S.; Zaki, R.; El Nady, M. M. Maastrichtian oil shale deposition on the southern Tethys margin, Egypt: Insights into greenhouse climate and paleoceanography. *Palaeogeogr. Palaeoclimatol. Palaeoecol.* **2018**, *505*, 18–32.
- (66) Qiu, X.; Liu, C.; Mao, G.; Deng, Y.; Wang, F.; Wang, J. Major, trace and platinum-group element geochemistry of the Upper Triassic nonmarine hot shales in the Ordos basin, Central China. *Appl. Geochem.* **2015**, *53*, 42–52.
- (67) Lerman, A. D. I.; Gat, J., Eds.; *Physics and Chemistry of Lakes*; Springer-Verlag: Berlin, 1989.
- (68) Föllmi, K. B. Early Cretaceous life, climate and anoxia. *Cretac. Res.* **2012**, *35*, 230–257.
- (69) Ma, B.; Ji, L.; Jin, P.; Zhang, M.; Yuan, B.; Long, L. Geochemical characteristics and depositional paleoenvironment of source rocks from the Lower Cretaceous Chijinbao Formation in Jiuxi Basin, China. *J. Petrol. Sci. Eng.* **2022**, *210*, No. 109968.
- (70) Tao, S.; Xu, Y.; Tang, D.; Xu, H.; Li, S.; Chen, S.; Liu, W.; Cui, Y.; Gou, M. Geochemistry of the Shitoumei oil shale in the Santanghu Basin, Northwest China: implications for paleoclimate conditions, weathering, provenance and tectonic setting. *Int. J. Coal Geol.* **2017**, *184*, 42–56.
- (71) Deng, S. H.; Lu, Y. Z.; Zhao, Y.; Fan, R.; Wang, Y. D.; Yang, X. J.; Li, X.; Sun, B. N. The Jurassic palaeoclimate regionalization and evolution China. *Earth Sci. Front.* **2017**, *24*, 106–142. (In Chinese)
- (72) Xu, Y.; Uhl, D.; Zhang, N.; Zhao, C.; Qin, S.; Liang, H.; Sun, Y. Evidence of widespread wildfires in coal seams from the Middle Jurassic of Northwest China and its impact on paleoclimate. *Palaeogeogr. Palaeoclimatol. Palaeoecol.* **2020**, *559*, No. 109819.
- (73) Xu, Z.; Cheng, Y.; Ao, C.; Zhang, T.; Wang, S. Middle Jurassic palaeoclimate changes within the central Ordos Basin based on palynological records. *Palaeobiodivers. Palaeoenviron.* **2023**, *103*, 21–42.
- (74) Guo, W.; Zhang, W.; Li, Y.; Lei, X.; Li, Y.; Chen, G.; Zhang, Y.; Chen, L.; Xu, X. Geochemistry of 7 Member Shale of the Dameigou Formation in the Northern Qaidam Basin, China: Significance and Implication for Provenance and Source Weathering in the Late Middle Jurassic. *Acta Sedimentol. Sin.* **2020**, *38*, 676–686. (In Chinese)
- (75) Liu, S.; Liu, B.; Tang, S.; Zhao, C.; Tan, F.; Xi, Z.; Du, F. Palaeoenvironmental and tectonic controls on organic matter enrichment in the Middle Jurassic Dameigou Formation (Qaidam Basin, North China). *Palaeogeogr., Palaeoclimatol., Palaeoecol.* **2020**, *585*, No. 110747.
- (76) Shao, J.; Yang, S.; Li, C. Chemical indices (CIA and WIP) as proxies for integrated chemical weathering in China: inferences from analysis of fluvial sediments. *Sediment. Geol.* **2012**, *265*, 110–120.
- (77) Lu, J.; Zhang, P.; Dal Corso, J.; Yang, M.; Wignall, P. B.; Greene, S. E.; Shao, L. Y.; Lyu, D.; Hilton, J. Volcanically driven lacustrine ecosystem changes during the Carnian Pluvial Episode (Late Triassic). *Proc. Natl. Acad. Sci. U. S. A.* **2021**, *118*, No. e2109895118.
- (78) Zhang, Z.; Li, H.; Zheng, W.; Whattam, S. A.; Zhu, Z.; Jiang, W.; Zhao, D. Response of Paleogene Fine-Grained Clastic Rock Deposits in the South Qiangtang Basin to Environments and Thermal

- Events on the Qinghai-Tibet Plateau. *ACS omega* **2023**, *8*, 26458–26478.
- (79) Lv, D.; Wang, L.; Isbell, J. L.; Lu, C.; Li, P.; Wang, Y.; Zhang, Z. Records of chemical weathering and volcanism linked to paleoclimate transition during the Late Paleozoic Icehouse. *Glob. Planet. Chang.* **2022**, *217*, No. 103934.
- (80) Fedo, C. M.; Wayne Nesbitt, H.; Young, G. M. Unraveling the effects of potassium metasomatism in sedimentary rocks and paleosols, with implications for paleoweathering conditions and provenance. *Geology* **1995**, *23*, 921–924.
- (81) Nesbitt, H. W.; Young, G. M. Prediction of some weathering trends of plutonic and volcanic rocks based on thermodynamic and kinetic considerations. *Geochim. Cosmochim. Acta* **1984**, *48*, 1523–1534.
- (82) Rimmer, S. M. Geochemical paleoredox indicators in devonian–Mississippian black shales, central appalachian basin (USA). *Chem. Geol.* **2004**, *206*, 373–391.
- (83) Yeasmin, R.; Chen, D.; Fu, Y.; Wang, J.; Guo, Z.; Guo, C. Climatic-oceanic forcing on the organic accumulation across the shelf during the early cambrian (age 2 through 3) in the mid-upper yangtze block, NE guizhou, south China. *J. Asian Earth Sci.* **2017**, *134*, 365–386.
- (84) Young, G. M.; Nesbitt, H. W. Processes controlling the distribution of Ti and Al in weathering profiles, siliciclastic sediments and sedimentary rocks. *J. Sediment. Res.* **1998**, *68*, 448–455.
- (85) Li, Q.; Wu, S. H.; Xia, D. L.; You, X. L.; Zhang, H. M.; Lu, H. Major and trace element geochemistry of the lacustrine organic-rich shales from the Upper Triassic Chang 7 Member in the southwestern Ordos Basin, China: implications for paleoenvironment and organic matter accumulation. *Mar. Petrol. Geol.* **2020**, *111*, 852–867.
- (86) Shaw, T. J.; Gieskes, J. M.; Jahnke, R. A. Early diagenesis in differing depositional environments: the response of transition metals in pore water. *Geochim. Cosmochim. Acta* **1990**, *54*, 1233–1246.
- (87) Algeo, T. J.; Maynard, J. B. Trace-element behavior and redox facies in core shales of Upper Pennsylvanian Kansas-type cyclothsems. *Chem. Geol.* **2004**, *206*, 289–318.
- (88) Algeo, T. J.; Ingall, E. Sedimentary C_{org} : P ratios, paleocean ventilation, and Phanerozoic atmospheric pO_2 . *Palaeogeogr. Palaeoclimatol. Palaeoecol.* **2007**, *256*, 130–155.
- (89) Ernst, T. W. *Geochemical Facies Analysis*; Elsevier: Amsterdam, 1970; p 152.
- (90) Jones, B.; Manning, D. A. Comparison of geochemical indices used for the interpretation of palaeoredox conditions in ancient mudstones. *Chem. Geol.* **1994**, *111*, 111–129.
- (91) Helz, G. R.; Miller, C. V.; Charnock, J. M.; Mosselmans, J. L. W.; Patrick, R. A. D.; Garner, C. D.; Vaughan, D. J. Mechanisms of molybdenum removal from the sea and its concentration in black shales: EXAFS evidences. *Geochim. Cosmochim. Acta* **1996**, *60*, 3631–3642.
- (92) Zheng, Y.; Anderson, R. F.; van Geen, A.; Fleischer, M. Q. Preservation of non-lithogenic particulate uranium in marine sediments. *Geochim. Cosmochim. Acta* **2002**, *66*, 3085–3092.
- (93) Algeo, T. J.; Liu, J. A re-assessment of elemental proxies for paleoredox analysis. *Chem. Geol.* **2020**, *540*, No. 119549.
- (94) Schenau, S. J.; Reichart, G. J.; De Lange, G. J. Phosphorus burial as a function of paleoproductivity and redox conditions in Arabian Sea sediments. *Geochim. Cosmochim. Acta* **2005**, *69*, 919–931.
- (95) Shen, J.; Schoepfer, S. D.; Feng, Q. L.; Zhou, L.; Yu, J. X.; Song, H. Y.; Wei, H. Y.; Algeo, T. Marine productivity changes during the end-Permian crisis and early Triassic recovery. *Earth-Sci. Rev.* **2015**, *149*, 136–162.
- (96) Schoepfer, S. D.; Shen, J.; Wei, H.; Tyson, R. V.; Ingall, E.; Algeo, T. J. Total organic carbon, organic phosphorus, and biogenic barium fluxes as proxies for paleomarine productivity. *Earth-Sci. Rev.* **2015**, *149*, 23–52.
- (97) Dymond, J.; Suess, E.; Lyle, M. Barium in deep-sea sediment: A geochemical proxy for paleoproductivity. *Paleoceanography* **1992**, *7*, 163–181.
- (98) Pfeifer, K.; Kasten, S.; Hensen, C.; Schulz, H. D. Reconstruction of primary productivity from the barium contents in surface sediments of the South Atlantic Ocean. *Mar. Geol.* **2001**, *177*, 13–24.
- (99) Reolid, M.; Rodríguez-Tovar, F. J.; Marok, A.; Sebane, A. The Toarcian oceanic anoxic event in the Western Saharan Atlas, Algeria (North African paleomargin): role of anoxia and productivity. *Geol. Soc. Am. Bull.* **2012**, *124*, 1646–1664.
- (100) Khan, M. Z.; Feng, Q.; Zhang, K.; Guo, W. Biogenic silica and organic carbon fluxes provide evidence of enhanced marine productivity in the Upper Ordovician-Lower Silurian of South China. *Palaeogeogr. Palaeoclimatol. Palaeoecol.* **2019**, *534*, No. 109278.
- (101) Wei, W.; Algeo, T. J. Elemental proxies for paleosalinity analysis of ancient shales and mudrocks. *Geochim. Cosmochim. Acta* **2020**, *287*, 341–366.
- (102) Wang, A.; Wang, Z.; Liu, J.; Xu, N.; Li, H. The Sr/Ba ratio response to salinity in clastic sediments of the Yangtze River Delta. *Chem. Geol.* **2021**, *559*, No. 119923.
- (103) Deng, H. W.; Qian, K. *Sedimentary Geochemistry and Environment Analysis*; GansuTechnology Publishing House: Lanzhou, 1993; pp 1–150 (in Chinese).
- (104) Qian, K.; Shi, H. The choice of the method of paleosalinity determination in resource evaluation. *Pet. Explor. Dev.* **1982**, *3*, 32–38. (In Chinese)
- (105) Berner, R. A.; Raiswell, R. C/S method for distinguishing freshwater from marine sedimentary rocks. *Geology* **1984**, *12*, 365–368.
- (106) Lee, K.; Kim, T. W.; Byrne, R. H.; Millero, F. J.; Feely, R. A.; Liu, Y. M. The universal ratio of boron to chlorinity for the North Pacific and North Atlantic oceans. *Geochim. Cosmochim. Acta* **2010**, *74*, 1801–1811.
- (107) McAlister, J.; Orians, K. Calculation of river-seawater endmembers and differential trace metal scavenging in the Columbia River plume. *Estuar. Coast. Shelf Sci.* **2012**, *99*, 31–41.
- (108) Remírez, M. N.; Algeo, T. J. Paleosalinity determination in ancient epicontinental seas: A case study of the T-OAE in the Cleveland Basin (UK). *Earth-Sci. Rev.* **2020**, *201*, No. 103072.
- (109) Carroll, A. R.; Bohacs, K. M. Stratigraphic classification of ancient lakes: balancing tectonic and climatic controls. *Geology* **1999**, *27*, 99–100.
- (110) Sageman, B. B.; Murphy, A. E.; Werne, J. P.; Ver Straeten, C. A.; Hollander, D. J.; Lyons, T. W. A tale of shales: the relative roles of production, decomposition, and dilution in the accumulation of organic-rich strata, Middle-Upper Devonian, Appalachian Basin. *Chem. Geol.* **2003**, *195*, 229–273.
- (111) Zhang, S. H.; Liu, C. Y.; Liang, H.; Wang, J. Q.; Bai, J. K.; Yang, M. H.; Liu, G. H.; Huang, H. X.; Guan, Y. Z. Paleoenvironmental conditions, organic matter accumulation, and unconventional hydrocarbon potential for the Permian Lucaogou Formation organic-rich rocks in Santanghu Basin. NW China. *Int. J. Coal Geol.* **2018**, *185*, 44–60.
- (112) Ding, J. H.; Zhang, J. C.; Huo, Z. P.; Shen, B. J.; Shi, G.; Yang, Z. H.; Li, X. Q.; Li, C. X. Controlling factors and formation models of organic matter accumulation for the Upper Permian Dalong Formation black shale in the Lower Yangtze region, South China: Constraints from geochemical evidence. *ACS omega* **2021**, *6*, 3681–3692.
- (113) Wei, H. Y.; Chen, D. Z.; Wang, J. G.; Yu, H.; Tucker, M. E. Organic accumulation in the lower Chihsia Formation (Middle Permian) of South China: constraints from pyrite morphology and multiple geochemical proxies. *Palaeogeogr. Palaeoclimatol. Palaeoecol.* **2012**, *353–355*, 73–86.
- (114) Warren, J. K. *Evaporites: Sediments, Resources and Hydrocarbons*; Springer: Berlin, 2016; pp 616–618.